# Modeling Emergent Behaviors of Multi-Cellular Systems in 3D Extracellular Matrix: Heterogeneous Extracellular Matrix Reconstruction, Cell Micromechanics and Novel Mechanotaxis

by

Hanqing Nan

A Dissertation Presented in Partial Fulfillment
of the Requirements for the Degree
Doctor of Philosophy

Approved April 2019 by the
Graduate Supervisory Committee:

Yang Jiao, Chair
Terry Alford
Houlong Zhuang

ARIZONA STATE UNIVERSITY

May 2019

ABSTRACT

Collective cell migration in the 3D fibrous extracellular matrix (ECM) is crucial to many physiological and pathological processes such as tissue regeneration, immune response and cancer progression. A migrating cell also generates active pulling forces, which are transmitted to the ECM fibers via focal adhesion complexes. Such active forces consistently remodel the local ECM (e.g., by re-orienting the collagen fibers, forming fiber bundles and increasing the local stiffness of ECM), leading to a dynamically evolving force network in the system that in turn regulates the collective migration of cells.

In this work, this novel mechanotaxis mechanism is investigated, i.e., the role of the ECM mediated active cellular force propagation in coordinating collective cell migration via computational modeling and simulations. The work mainly includes two components: (i) microstructure and micromechanics modeling of cellularized ECM (collagen) networks and (ii) modeling collective cell migration and self-organization in 3D ECM. For ECM modeling, a procedure for generating realizations of highly heterogeneous 3D collagen networks with prescribed microstructural statistics via stochastic optimization is devised. Analysis shows that oriented fibers can significantly enhance long-range force transmission in the network. For modeling collective migratory behaviors of the cells, a minimal active-particle-on-network (APN) model is developed, in which reveals a dynamic transition in the system as the particle number density $\rho$ increases beyond a critical value $\rho_c$, from an *absorbing* state in which the particles segregate into small isolated stationary clusters, to a *dynamic* state in which the majority of the particles join in a single large cluster undergone constant dynamic reorganization. The results, which are consistent with independent experimental results, suggest a robust mechanism based on ECM-mediated mechanical coupling for collective cell behaviors in 3D ECM.

For the future plan, further substantiate the minimal cell migration model by incorporating more detailed cell-ECM interactions and relevant sub-cellular mechanisms is needed, as well as

further investigation of the effects of fiber alignment, ECM mechanical properties and externally applied mechanical cues on collective migration dynamics.

ACKNOWLEDGMENTS

I am indebted to a number of people who have made my stay at Arizona State University both productive and enjoyable. I thank my family and friends for their support and love, without which I could not have finished this dissertation.

I am sincerely grateful and deeply indebted to my advisor Dr. Yang Jiao, for his continued intellectual and professional guidance and his sincere care for my research. I also sincerely thank my committee members Dr. Terry Alford, Dr. Xiao Wang and Dr. Houlong Zhuang for their guidance and suggestions for my research. My work would not have been possible without close collaboration with my lab mates Dr. Wenxiang Xu, Dr. Hechao Li, Dr. Shaohua Chen, Dr. Long Liang, Dr. Yaopengxiao Xu, Pei-En Chen and Yu Zheng.

TABLE OF CONTENTS

Page

CHAPTER Page

LIST OF TABLES

Table Page

LIST OF FIGURES

Figure Page

Figure Page

Figure Page

Figure Page

Figure Page

Figure Page

Figure Page

Figure Page

# CHAPTER 1

# INTRODUCTION

## 1.1 Extracellular matrix and its models

The extracellular matrix (ECM) is an interconnected network of biopolymers mainly composed of type I collagen (COL-I) that provides structural support for cells and allows the diffusion of biochemicals within tissues [1]. Cells attach to and move through the ECM using protein complexes that link the ECM to the force-generating cell cytoskeleton [2]. These cell-ECM adhesions also act as sensors, allowing cells to respond to the local microstructure and mechanical properties of the surrounding ECM [3,4] and regulating various cell behaviors [5–7]. The stiffness and the relative alignment of fibers in the network are particularly important to cell function. For example, dense and rigid collagen gel can promote growth and progression of cancer cells and tumors [8,9]. For example, the stiffness and alignment of collagen fibers in the ECM can significantly affect cellular migration, via durotaxis (i.e., cells tend to move in the direction of increasing matrix stiffness) [10] and contact guidance (i.e., cells tend to move in the direction of fiber alignment) [11,12].

On the other hand, active cells can remodel the network [4,13,14] and even affect the bulk properties of the ECM [15–18]. Specifically, the tension exerted by the cells can align the fibers in the network leading to long-range force transmission [15,19–22]. Fiber mediated stresses can in turn trigger mechanosensitive pathways for regulating collective cell dynamics [23–29]. This coupling of cells provides a means for mechanical communication and plays an important role in regulating and coordinating collective cellular dynamics in a wide range of biophysical processes, such as morphogenesis, tissue regeneration, and immune response, as well as diseases such as muscular dystrophy, fibrosis, and cancer [4,13,30–34].

Due to their effects on cell behavior and communication, a significant amount of work has been carried out to characterize the structural and physical properties of biopolymer ECM networks.

Traditional morphological descriptors for such networks include the distribution of fiber length [35], porosity [36,37], pore-size distribution [38–41], and turbidity [42,43], which are mainly bulk averaged properties. Recently, local topological and geometrical statistics such as the distribution of numbers of fibers at a cross-link node (i.e., valence number) and relative fiber orientations (i.e., direction cosine) are employed to successfully reconstruct COL-I network computationally [44]. Higher order spatial fluctuations have also been utilized to characterize the evolution of COL-I network during the gelation process [45]. In addition, the transport properties (e.g., macromolecule diffusivity) [41,46–54] and mechanical properties (e.g., elastic moduli, bulk rheology, stress distribution, etc.) [15,19,44,55–61] of biopolymer networks, which are respectively crucial to the chemical and mechanical signaling between the cells, strongly depend on the network microstructure. In addition, stress heterogeneity and strain localization of collagen networks especially when interacting with cells have been systematically investigated [62–64].

In the past decade, a variety of discrete fiber-based models have been devised to investigate the mechanical behavior and force transmission in polymer networks [15,22,61,65–69]. It is found that under both global and local perturbations, a 2D random network can exhibit both non-affine and affine deformation regimes, which are respectively bending and stretching dominant [65,66]. The distribution of forces in the network is highly heterogeneous, with the majority of forces carried by a small fraction of fibers [65]. Very recently, force transmission in the cellularized network has been studied using model random networks and cells in 2D [21,61,68]. It has been shown that a contractile elliptical cell can lead to highly heterogeneous force networks in a random network and result in significant fiber orientation [15]. Importantly, the remodeled network supports the transmission of cell-generated forces over a distance that is one order of magnitude larger than the linear cell size, suggesting fiber-mediated long-range mechanical signaling between distant cells [61,68]. In addition, the relation between the range of force transmission and cell morphology has been elucidated [61].

In spite of the exciting progress in understanding the dynamic cell-ECM interactions, the effects of microstructural heterogeneity of the ECM have not been systematically investigated. The preponderance of the aforementioned studies has employed relatively simple model networks with

the artificial geometrical or topological disorder. Recently, a stochastic reconstruction method has been devised that allows one to generate virtual collagen networks possessing prescribed local topological and geometrical statistics associated with actual collagen networks [44]. Such statistics include the valence number distribution (i.e., the number of fibers at a cross-link node), fiber length distribution, and fiber orientation (i.e., direction cosine) direction, which can be computed from 3D confocal images of the network of interest. However, the reconstructed virtual networks are spatially homogeneous, i.e., the prescribed statistics are invariant at different locations of the systems, which might not fully capture the nature of the *in vivo* microenvironment.

### 1.2 Reconstruction of collagen-based extracellular matrix

Very recently, an *in vitro* model of 3D ECM containing metastatic breast cancer (MDA-MB-231) cells have been constructed in order to investigate the effect of ECM heterogeneity on cancer invasion [70]. The model ECM contains a collagen region with either randomly orientated or aligned collagen fibers, which is attached to a layer of dense Matrigel, shown in *Figure 1.1*. This is to mimic the stroma surrounding a breast tumor which includes both remodeled collagens as well as dense basal membranes. As the first step for leaving the primary tumor and entering into the circulation system, the invasive cells need to penetrate the dense basal membranes. It has been shown in this *in vitro model* the tumor cells in the ECM with prealigned fibers can easily penetrate deeply into the dense Matrigel region, while the same cells in random ECM cannot. This observation has led to the conclusion that oriented collagen fibers can significantly enhance tumor cell intravasation. However, the mechanism for this new paradigm is not fully understood yet.

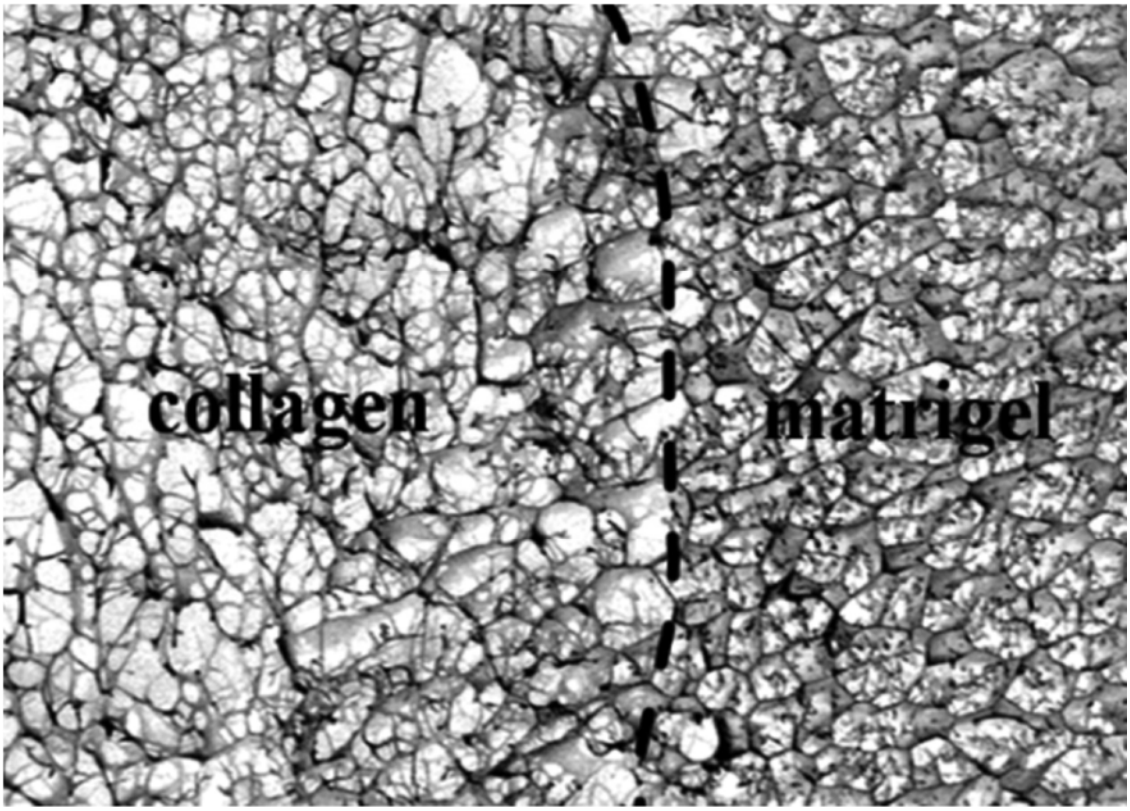


*Figure 1.1 Scanning electron microscopy (SEM) image showing the microstructure of the model heterogeneous ECM which contains a collagen region (left part) attached to a layer of dense Matrigel (right part).*

We propose to carry out a systematic numerical investigation to understand the mechanism under the enhanced tumor cell intravasation by aligned fibers. The step is to generate realizations of collagen-based ECM with high spatial heterogeneity, in order to mimic the in vitro environment. To this end, we develop a computational framework to investigate force generation and propagation in 3D heterogeneous ECM containing migrating breast cancer cells.

As a first step towards a better understanding of the mechanisms underlying the enhanced tumor cell intravasation by aligned collagen fibers, we develop a procedure for generating realizations of highly heterogeneous 3D collagen networks with prescribed microstructural statistics via stochastic optimization, which generalizes the framework devised in reference [44].

Specifically, a correspondence between microstructure and micromechanics of cellularized 3D ECM is established. By extracting statistical geometrical and topological information of the ECM structure from the limited confocal images, collagen networks with different morphological features (e.g., collagen fiber orientations), an ECM designed for the migrating cells are reconstructed.

We note that ECM is an intrinsic heterogeneous material. For example, the local cross-link (node) density, the coordination (valence) number at each node, and the fiber orientations are all varying at different locations of the system. By *highly heterogeneous*, we mean that besides the intrinsic spatial variation of the aforementioned local properties, the system also includes large and abrupt changes of local properties (e.g., the fiber orientations) as observed in the *in vitro* ECM constructed in reference [70]. In this work, a collagen network is represented via the graph (node-bond graph) model and the microstructural statistics considered include the *spatial-location dependent* cross-link (which is a node) density, valence distribution, fiber (which is bond) length distribution, as well as fiber orientation distribution. An optimization problem is formulated in which the objective function is defined as the squared difference between a set of target microstructural statistics and the corresponding statistics for the simulated network. Simulated annealing is employed to solve the optimization problem by evolving an initial network via random perturbations in order to match the specific statistics in different regions of the system to generate realizations of desirable networks. This procedure is employed to render realizations of homogeneous networks with randomly oriented fibers, homogeneous networks with aligned fibers, heterogeneous networks with a continuous variation of fiber orientation along a prescribed direction, as well as a binary system containing a collagen region with aligned fibers and a dense Matrigel region with randomly oriented fibers.

### 1.3 Micro-mechanical analysis of reconstructed ECM containing contractile cells

A force network of the given ECM is established for identifying the mechanical feedback between an isolated contractile cell and its local ECM. In particular, the network fibers in the vicinity of the cell surface are attached to the cell, whose deformation induces displacement boundary conditions for the fibers. The generation and propagation of active forces in the virtual ECM networks due to polarized contraction of an embedded ellipsoidal cell are analyzed by considering a nonlinear fiber model. Specifically, the fiber's constitutive relation incorporates strain hardening upon large stretching and buckling upon compression. A nonlinear constitutive fiber micromechanical model is employed, which considers buckling upon compression and strain-hardening upon stretching. The effects of ECM microstructure on the force network generated due to a migrating cell are studied as well. The migrating cells regulate and coordinate with one another via ECM mediated force generation and propagation, leading to possible collective invasive behaviors *in vivo*.

Our analysis shows that oriented fibers can significantly enhance long-range force transmission in the network. Moreover, this conclusion matches the results gains from the experiment very well. In the oriented-collagen-Matrigel system, the forces generated by a polarized cell in collagen can penetrate deeply into the Matrigel region. Such stressed Matrigel fibers could provide contact guidance for the migrating cells, and thus enhance their penetration into Matrigel. This suggests a possible mechanism that could explain the nature of enhanced tumor cell intravasation observed in oriented collagen interfaces. We also investigate the propagation of active forces generated by a small group of cells in the ECM with varying degree of heterogeneities, to mimic the collective contraction of the invasion front of the *in vitro* tumor.

### 1.4 MRJ packing

In the subsequent simulations, we will construct model networks based on maximally random jammed (MRJ) packings of equal-sized hard spheres in 3D. These packings are isostatic and disordered, and thus, provide an ideal system when concerted a disordered network, for our investigation of collective cell dynamics on the network. In particular, starting from a low-density configuration of small non-overlapping spheres randomly distributed in the simulation box, each sphere is given a random velocity. The particles follow Newton's law of motion, colliding with each other as they move and each particle also grows (i.e., isotopically expand) with a prescribed growth rate. The simulated is terminated once a jammed packing of the spheres, characterized by a diverging collision rate, is obtained

### 1.5 Collective cell migration

Collective cell migration in the 3D fibrous extracellular matrix (ECM) is crucial to many physiological and pathological processes such as tissue regeneration, immune response and cancer progression [30,71–73]. Cell migration is a complex dynamic process involving a series of intracellular and extra-cellular activities including the development of filopodia, formation of focal adhesion sites, locomotion due to actin filament contraction, and detachment of the rear end [2,74]. Besides the well-established chemotaxis [75], the microstructure and physical properties of the ECM network [17,41,44,76–79] (mainly composed COL-I) can also significantly influence single cell migration via durotaxis [34,80], haptotaxis [81], and contact guidance [12,82]. For example, in durotaxis, a cell can sense and respond to the rigidity gradient in the local microenvironment, which in turn guides its migration.

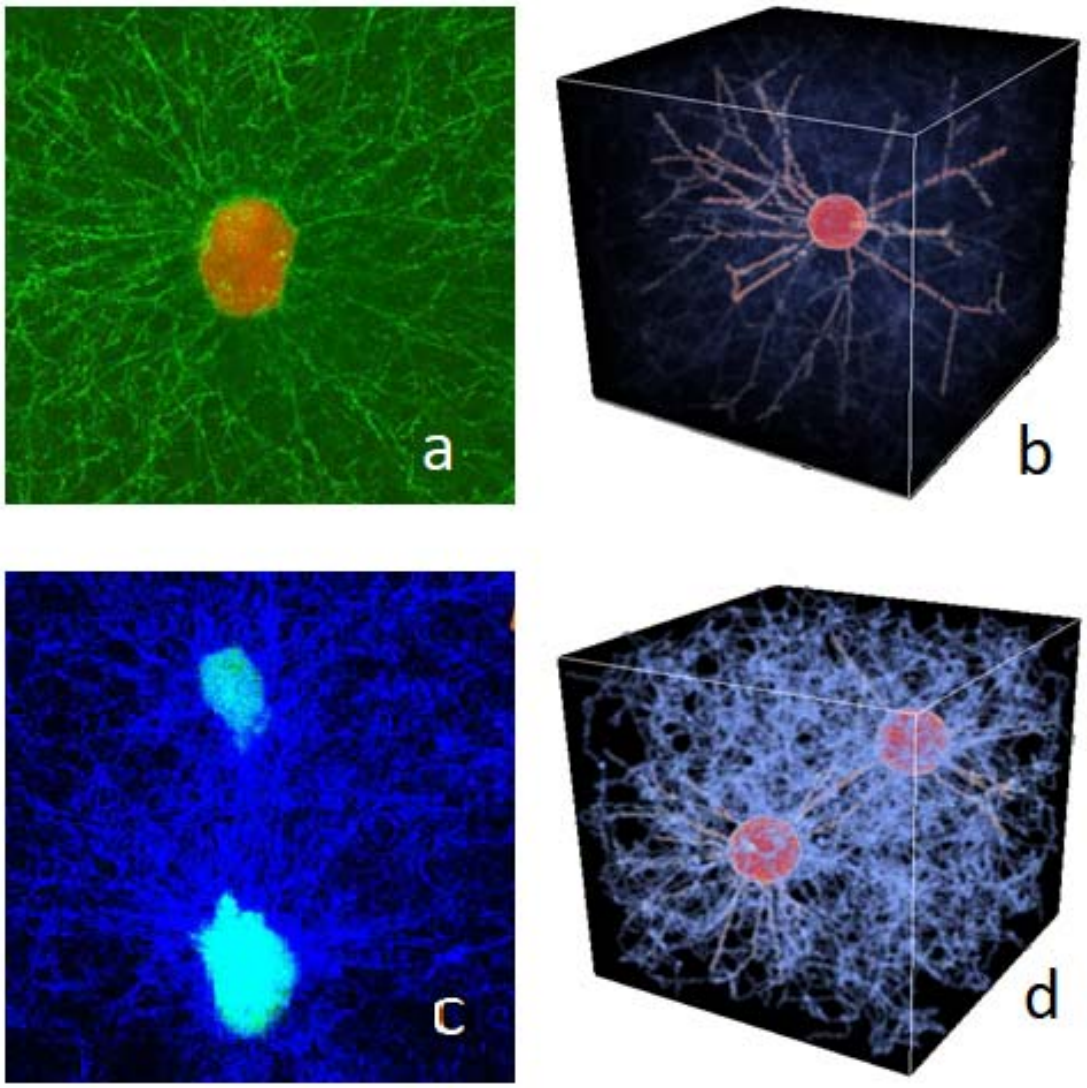


*Figure 1.2 (a) Confocal image of a single contractile cell, generating active forces that re-align the ECM fibers (bright green) along the radial directions. (b) Simulated force chain (highlighted in red) resulted from a single contractile cell (represented as a red sphere) in the 3D ECM network. (c) Confocal image of a multi-cellular system with stress-fiber bundles (bright blue) between contractile cells. (d) Simulated force network (highlighted in red) resulted from two migrating contractile cells. The linear size of the images is roughly 100 microns in all cases.*

During migration, individual cells can generate active pulling forces via actin filament contraction [83], which are transmitted to the ECM fibers via the focal adhesion complexes [23,25,84,85]. Such active forces can remodel the local ECM (e.g., by re-orienting the collagen fibers), which in turn facilitate the long-range propagation of the forces to distant sites [15,18,19,21], shown in *Figure 1.2(a)* and *Figure 1.2(b)*. Recent studies have indicated that a delicate balance among the magnitude of the pulling forces, the cell-ECM adhesion strength, and ECM rigidity is required to achieve an optimal mode of single cell migration [27].

In a multi-cell system, the pulling forces generated by individual cells can result in a dynamically evolving force network in the ECM, shown in *Figure 1.2(c)* and *Figure 1.2(d)*. Since cells can sense and respond to the stress state of their local microenvironment [28] and adapt their migratory behaviors accordingly [27], the dynamic force network can further influence the migration of the individual cells, leading to various collective dynamics. Such collective dynamics, in turn, would remodel the force network. This feedback loop between the force network and cell migration could lead to rich collective migratory behaviors. This could offer a novel mechanism for collective cell behaviors besides local cell-cell interactions and those based diffusive factors [86–91]. For example, in a recent *in vitro* experiment, an abnormal and rapid aggregation of invasive breast cancer cells (in contrast to random spreading) during a massive polarized invasion has been observed, which was resulted from the strong ECM-mediated mechanical coupling among the cancer cells induced by the collective polarization

Although there is increasing experimental evidence indicating the important role of the dynamic force network in multi-cellular ECM systems, a comprehensive theory and quantitative framework for understanding and predicting emergent collective cellular dynamics resulted from the force network in 3D ECM have not to be established. General organizational principles for various emergent collective behaviors in multicellular ECM systems remain to be elucidated. The effects of the geometry and topology of the ECM network, its mechanical properties, as well as external mechanical cues on the force network and the resulting emergent cellular behaviors are not well understood.

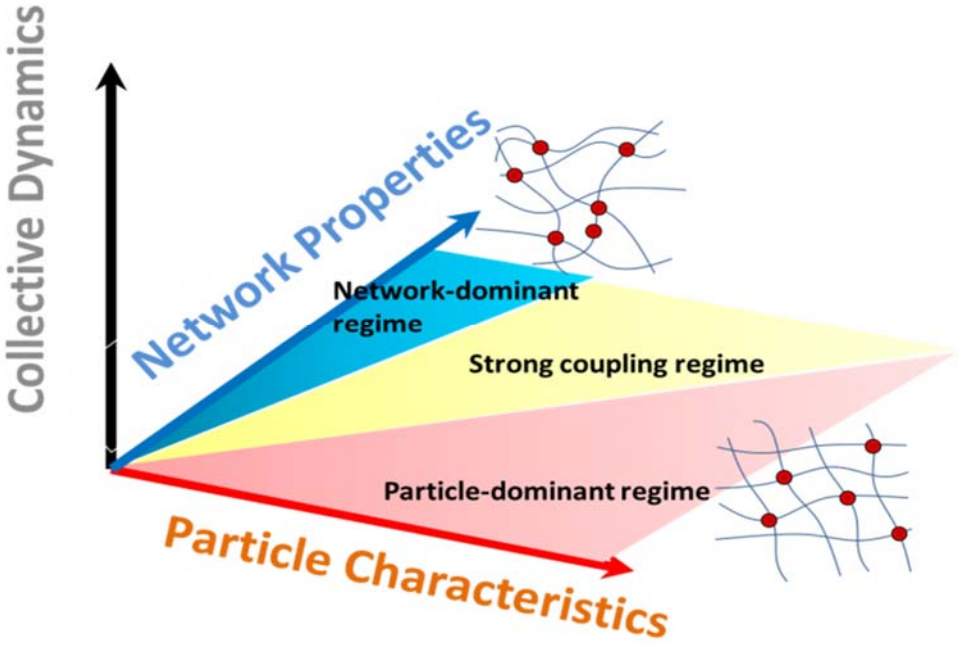


*Figure 1.3 A hypothetical phase diagram of the collective dynamics (e.g., segregation vs. clustering, jamming vs. collectively migrating etc.) in the active-particle-on-network (APN) system. Depending on the properties of the ECM and characteristics of the particles, the system can be network-dominant, particle-dominant or in a strong particle-network coupling regime.*

### 1.6 Active-particle-on-network model

We have established a computational model by investigating the role of the dynamic force network in regulating collective cellular behaviors in 3D ECM, via a minimal active-particle-on-network (APN) model. In this model, the active particles (representing contractile cells) can occupy a subset of the nodes of a network, pull the fibers connected to the occupied node, and hop between neighboring nodes depending on the stress state of the fiber connecting the nodes. Despite its simplicity, we expect to elucidate general mechanical organizational principles for the emergent collective behaviors using the APN model. We will investigate the role of the microstructure and

mechanical properties of the ECM network as well as the role of external mechanical cues in regulating the force network and the resulting emergent cellular behaviors. In particular, we envision a hypothetical *phase diagram*, shown in *Figure 1.3*, of the collective dynamics, e.g., segregation vs. clustering, jamming vs. collectively migrating etc., which, depending on the properties of the ECM and characteristics of the particles, can be network-dominant, particle-dominant or in a strong particle-network coupling regime. This hypothesis will be tested throughout the project. In addition, we will develop a novel framework and metrics for quantifying the dynamics of APN systems and a mean-field theory for the observed emergent behaviors. The generality and applicability of the minimal APN model will be tested using a more comprehensive model taking to account various inter-cellular and cell-ECM interactions. Comparisons with experimental results will be made whenever possible for validating the theory.

The rest of the dissertation is organized as follows: In Chapter 2, we will focus on stochastic reconstruction of extracellular matrix for micro-mechanical analysis of tumor cell invasion, mostly described detailed network statistics, the formulation of the stochastic reconstruction procedure, as well as the mechanical model for cell-ECM mechanical interaction analysis. In Chapter 3, we report a novel active-particle-on-network model which designed for characterizing three-dimensional collective cell migration coordinated by micromechanical environment of ECM. In Chapter 4, we provide our plan for future work.

# CHAPTER 2

# STOCHASTIC RECONSTRUCTION OF EXTRACELLULAR MATRIX FOR MICRO-MECHANICAL ANALYSIS OF TUMOR CELL INVASION

## 2.1 Sample preparation and statistics extraction for reconstruction from collagen network

The original collagen network used is prepared in the following method described below [21]. The gels were prepared from high-concentration rat tail collagen-I in acetic acid (Corning, 10 mg·mL$^{-1}$). The collagen was diluted with $dH_2O$, 5× phosphate buffered saline (PBS), and 0.1 mol·L$^{-1}$ NaOH to final concentrations of 1 mg·mL$^{-1}$ and a pH of 7.4. The gelation temperature is 35 °C, which was regulated using a stage top incubator (ibidi Heating System, universal fit) equipped with an external temperature sensor (thermocouple type-K). Confocal reflection microscopy images of the collagen gel were taken using an inverted laser scanning confocal microscope (LSCM, Leica TCS SPE) with a 20× oil immersion objective. Samples were illuminated with a 532 nm laser and reflected light passed through a 30/70 RT filter and confocal pinhole before being collected by a photomultiplier tube detector (PMT). The scan size was 1024 × 1024 pixels (367 μm × 367 μm) and reflected light intensity was collected as 8-bit grayscale images. One confocal z-stack was taken for the collagen sample with the first scan ~ 10 μm above the glass to avoid reflection interference. 100 scans were taken per well with a 1.7 μm z-spacing between each scan.

The individual scans (i.e., 2D slices) were then stacked along the z-direction using ImageJ, to render a digitized volume of the collagen gel. In the 3D volume, the grayscale value of a voxel (i.e., the 3D analogy of a pixel) indicates the local reflection intensity and thus, whether that voxel belongs to a collagen fiber or the interstitial liquid. A dilation–erosion method [92–94] is then employed to extract the skeleton of the collagen network. Specifically, the 3D volume is thresholded to generate a binary field with black voxels indicating the *collagen phase*. The collagen phase is then dilated by adding another layer of black voxels on top of fiber surface voxels to preserve the

connectivity of the network. Then the collagen phase is eroded by iterative removing layers of black voxels, while maintaining the connectivity of the network. The skeletonized network is then converted to the graph (bond-node) model [44], in which a node represents a crosslink and a bond connecting a pair of nodes represents a segment of a collagen fiber between two crosslinks. We emphasize that the resolution limit of our confocal microscopy is about 300 nm and that collagen fibrils with a thickness less than this value cannot be well resolved and reconstructed. In our subsequent modeling, we only explicitly consider the thick fiber bundles that can be well resolved using our confocal microscopy. One way to take into account the effects of the finer background fibers is to employ an effective-medium approach and treat the fibers as a continuum with effective elastic properties that coupled of the discrete thick fiber bundles explicitly considered in our current model.

In the model extracted from the 3D stacks of the confocal image, information of the collagen is extracted into two abstracted objectives: fiber and node. And a 3D ball-and-stick model, see *Figure 2.1*, is used to represent the network for visualization purposes. In the model, a fiber is defined as single collagen fiber with two endpoints. And a node is the representative of the sharing endpoint of different fibers. A valence is assigned to each node indicating the number of fibers connected to. The collagen fibers that display in 3D confocal image stack is processed into abstracted 3D geometrical information of a typical collagen-based ECM network.

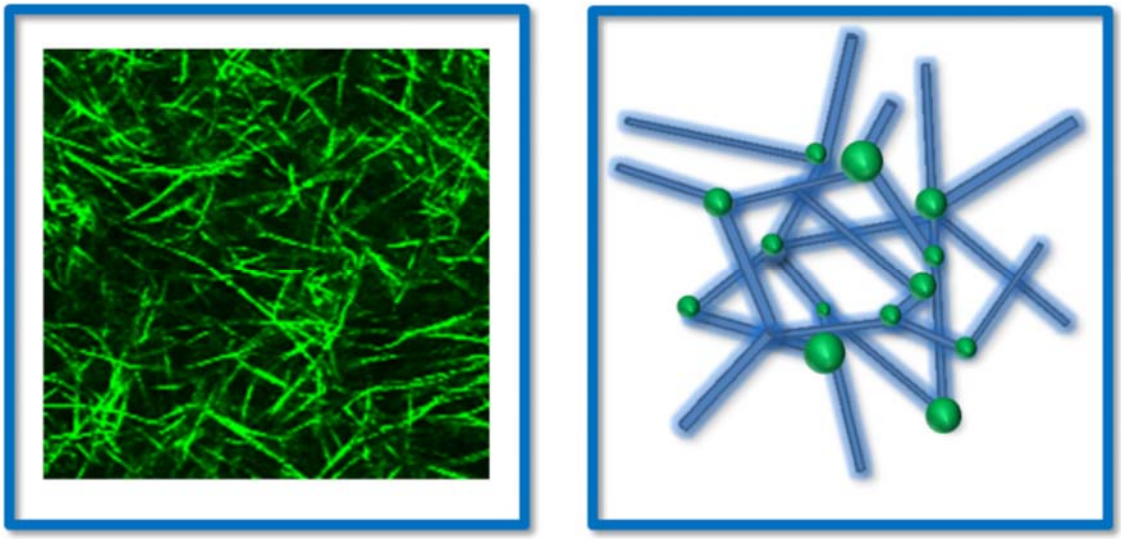


*Figure 2.1 Schematic illustration of the bond-node mode (b) for a collagen network derived from its confocal image (a).*

Some critical geometrical information extracted from the rendered 3D stack image of confocal microscopy is shown in *Table 2.1*. The concentration of collagen fiber in the ECM network is 1 mg/mL. The average node valence is 3.38. And the average fiber length is 1.96 micron. The orientation of the fiber is also monitored. To get numerical data of the orientation distribution of the fibers, absolute value of direction cosine of the angle between the fiber and z-axis is calculated as the descriptor. It is obvious that in the original network measured from experimental images, the average direction cosine should be 0.5 which indicates that orientation of the fiber is not controlled, in another word, randomly distributed. This geometrical information as long as the topological information extracted from the original collagen-based ECM network will be used as the basis of the reconstructed network, or in another word, the original dataset of the reconstruction.

| | |
|---|---|
| Concentration of collagen *fiber* in the network | 1 mg/mL |
| Average *node* valence | 3.38 *fiber*/*node* |
| Average *fiber* length | 1.96 micron |
| Average absolute direction cosine | 0.500 |

*Table 2.1 Geometric information extracted from rendered 3D stacked confocal image*

Despite the average of node valence and average of fiber length, we also extract more refined statistics such as the distribution of the node valence and the distribution of the fiber length. *Figure 2.2(a)* and *Figure 2.2(b)* shows the valence distribution and fiber length distribution extracted from the 3D stacked confocal image, respectively. These two datasets are also used as the original datasets of the reconstructed network.

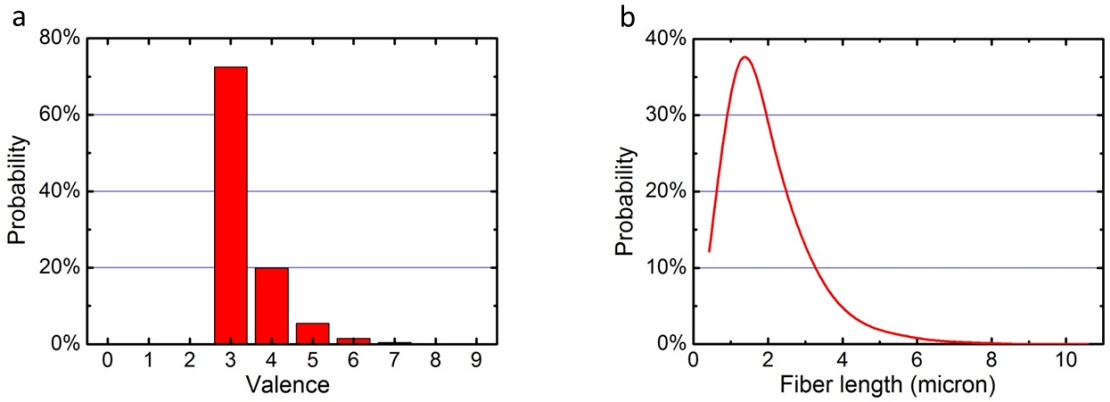


*Figure 2.2 The distribution obtained from experimental grown ECM; (a) valence distribution; (b) length distribution*

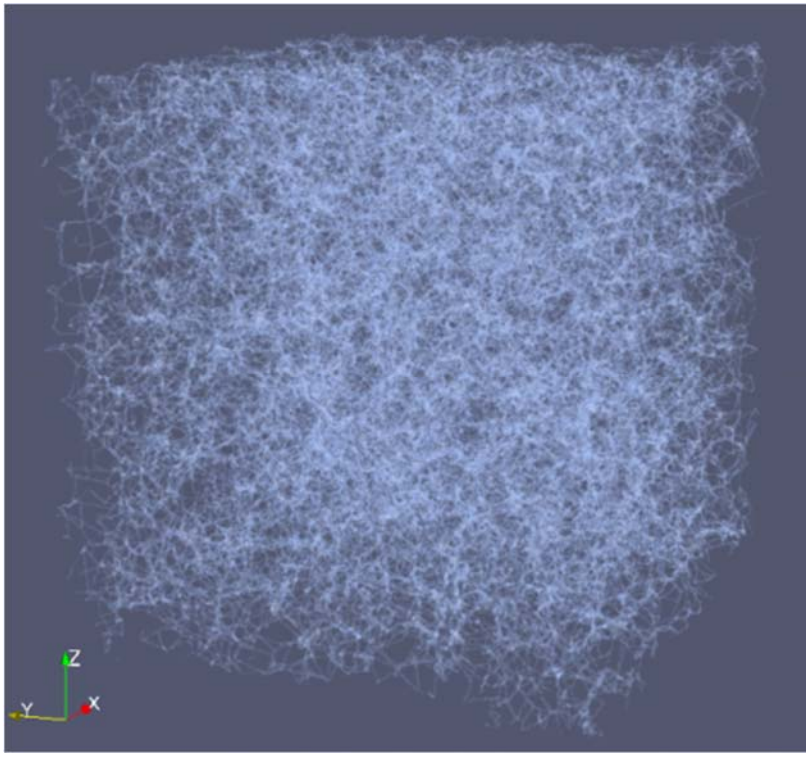


*Figure 2.3 ECM network reconstructed using dataset extracted from the original experimental ECM network*

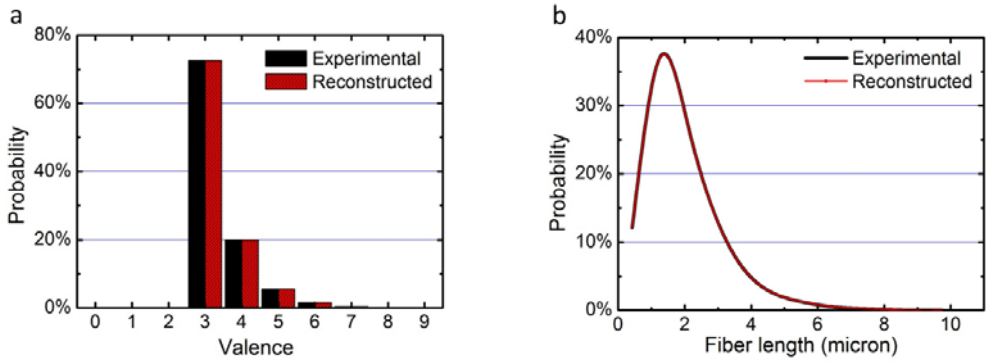


*Figure 2.4 The comparison of datasets between distributions extracted from experiment and from reconstructed; (a) valence distribution; (b) length distribution*

In order to test the method that can reconstruct the collagen-based ECM network, we put in the extracted statistics to rebuild a network with the same parameter of the original network. After the node and fiber information is extracted from the 3D stacked confocal image, a ball-and-stick model is applied to visualize the collagen-based ECM network. *Figure 2.3* shows a reconstructed collagen-based ECM with parameters from the extracted statistics in our modeling. The reconstructed network is 10 times larger than the original network we use to extract the original datasets. In this way, we can simulate a network with very same geometrical and topological properties but enlarge the size of the network to involve in more microstructures in the model.

Furthermore, the reconstructed collagen-based ECM network shares the same geometrical and topological properties are verified in *Figure 2.4*. *Figure 2.4* shows the comparison of distributions between the experimentally-built original network and the reconstructed network. The left panel shows the valence distribution comparison. The right panel compares the difference in length distribution. We can observe that the reproduction of the network is perfect as both the valence distribution and fiber length distribution would match. In the fiber length distribution, the two curves overlap with each other.

In the next section, we will introduce how is the network is reconstructed using stochastic optimization.

### 2.2 Reconstruction of collagen-based ECM using stochastic optimization

The method we use to reconstruct the collagen-based ECM network is based on the stochastic optimization procedure devised by Yeong and Torquato [95,96]. The overall network reconstruction procedure based on stochastic optimization is illustrated in *Figure 2.5*.

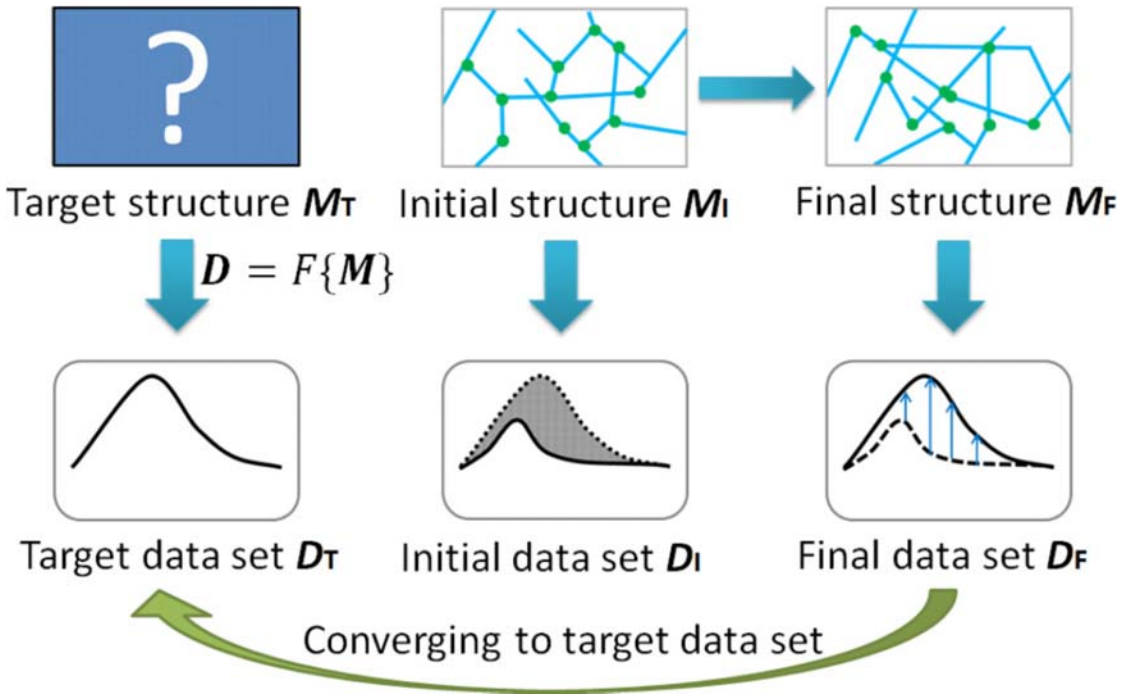


*Figure 2.5 Schematic illustration of the overall network reconstruction procedure based on stochastic optimization.*

Considering a 3D collagen-based ECM network $\boldsymbol{M}$, an experiment that performed to probe the structure of the network $\boldsymbol{M}$ will generate a set of data $\boldsymbol{D}$ that related to its structure. A mathematical transformation F could be defined so that the structure could be mapped:

$$\boldsymbol{D} = F\{\boldsymbol{M}\}$$

For example, the structural data set $\boldsymbol{D}$ contains spatial statistics sampled from the original 3D collagen-based ECM network when $\boldsymbol{M}$ is the network extracted from the experimental 3D image. Key statistic parameters are extracted from the experimental-built collagen-based ECM network including the concentration of the collagen involved in the network $C_0$, valence distribution of the nodes $\boldsymbol{V}$ (number of fibers that a node is connected to), the length distribution of the fibers $\boldsymbol{L}$ and the orientation of the fibers $\boldsymbol{S}$.

$$\boldsymbol{D} = \{C_0, \boldsymbol{V}, \boldsymbol{L}, \boldsymbol{S}\}$$

The reconstruction of the collagen-based ECM network involved two steps: the first step is to rebuild the geometry of the network with a maintained concentration of fiber. In this step, the concentration of the fiber is reproduced by adding a certain number of nodes with given valence into the system. Then, the nodes are connected by fibers following the given valence simultaneously. Hence, a network with a matched concentration of fiber and fixed topology is built. This network is denoted as $\boldsymbol{M_{initial}}$. And the network will be used as an initial structure in the following step.

In the second step, the length distribution and spatial distribution is matched by stochastic optimization. To reconstruct a 3D collagen-based ECM with target geometry dataset, a generalized Yeong-Torquato [95,96] procedure is devised. In particular, the reconstruction problem is formulated as an *objective function* minimization problem. Here, the objective function could be treated as the virtual energy of the system. The objective function is defined as the sum of squared differences of datasets between the target one $\boldsymbol{D}$ and a corresponding one measured from a trial $\boldsymbol{D^*}$.

$$E = |\boldsymbol{D} - \boldsymbol{D}^*|^2$$

Where $\boldsymbol{D} = F\{\boldsymbol{M}\}$ and $\boldsymbol{D}^* = F\{\boldsymbol{M}^*\}$

The square difference could be defined as the sum of the squared differences between corresponding data points in $\boldsymbol{D}$ and $\boldsymbol{D^*}$.

With the equation above, the problem of reconstruction of 3D collagen-based ECM will be transferred into a numerical problem that could be solved as a simulated annealing method [95]. Specifically, starting from the initial trial structure $\boldsymbol{M_{initial}}$ of the ECM network, which contains a fixed number of nodes and fibers, $\boldsymbol{M_{old}}$ is defined as the old structure of the ECM network. And then, a randomly selected node is selected to move to a random position adjacent to its neighbor. Thus, a new structure of $\boldsymbol{M_{new}}$ is formed. Both transformation of $\boldsymbol{M_{old}}$ and $\boldsymbol{M_{new}}$ is obtained as associated data set $\boldsymbol{D_{old}}$ and $\boldsymbol{D_{new}}$, where $\boldsymbol{D_{old}} = F\{\boldsymbol{M_{old}}\}$ and $\boldsymbol{D_{new}} = F\{\boldsymbol{M_{new}}\}$.

$\boldsymbol{D}_{old}$ and $\boldsymbol{D}_{new}$ are then compared to the experimentally measured structural data $\boldsymbol{D}$. The energies $E_{old}$ and $E_{new}$, which are associated with the old and new trial structures, repressively, are then evaluated using the equation:

$$E = |\boldsymbol{D} - \boldsymbol{D}^*|^2.$$

The values of objective function determine whether the new trial microstructure should be accepted or not via the probability:

$$p_{acc}(old \rightarrow new) = \min\{1, \exp(\frac{E_{old}}{T})/\exp(\frac{E_{new}}{T})\}$$

Where T is a virtual temperature that is chosen to be initially high and slowly decreases according to the annealing schedule. See the schematic illustration of *Figure. 2.5*. The whole reconstruction is divided into different stages. Each stage will have a separated virtual temperature. The reduce strategy of virtual temperature is shown in *Figure. 2.6*. Here, the virtual temperature is reduced exponentially as the reconstruction stage goes.

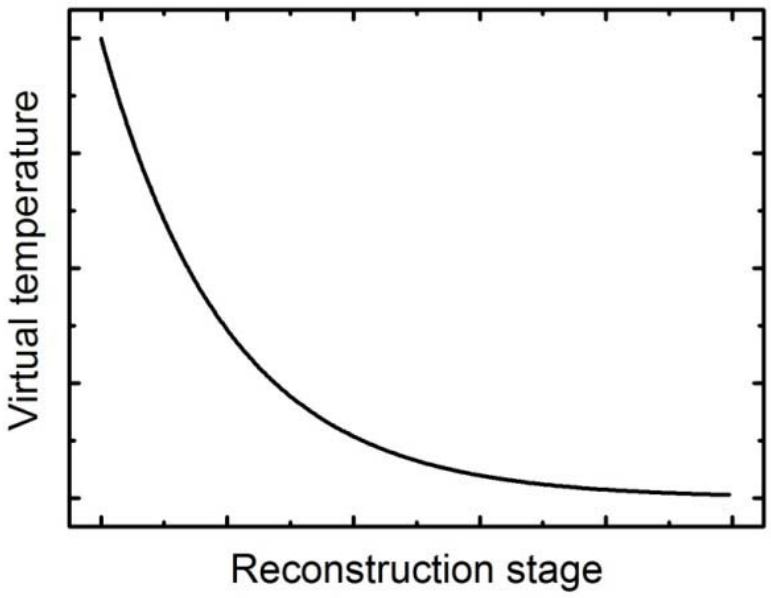


*Figure 2.6 The virtual temperature reduce with the reconstruction stage*

The whole reconstruction is divided into different stages. Each stage will have a separated virtual temperature. And for each stage, the objective function will be converged in finite steps before the posterior stage. At the beginning stages of the convergence, the virtual temperature is selected at a relatively high level which allows the formation of objective function up-hill structures. An acceptance rate will be calculated in each stage in order to keep track of these up-hill transformations. Higher the acceptance rate, more up-hill transformations occur in the stage. As the temperature gradually decreases, this up-hill movement is less favorable which would decrease the chance that the objective function would escape from the local minimum. Thus, it is very difficult to reduce the objective function of a system that approaches its possible global minimum practically. So when the objective function reaches as low as an acceptable prescribed tolerance, the annealing process is considered complete, see *Figure 2.7*.

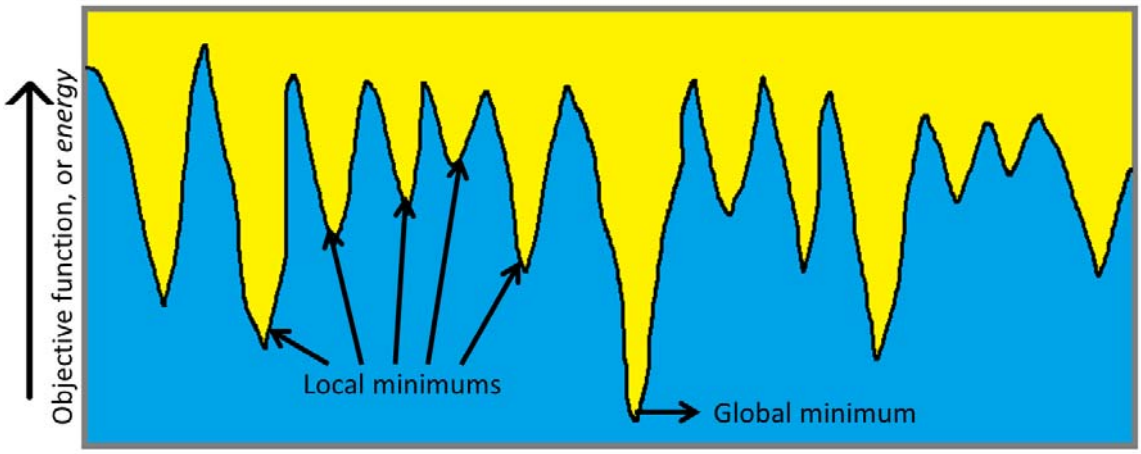


*Figure 2.7 Schematic illustration of the simulated annealing reconstruction procedure. The acceptance of the trial with the increasing objective function will allow the system to escape from the local minimum which would gain the probability to converge to the global minimum.*

This would allow the system approaches a local minimum that infinitely reaches its global minimum when the tolerance is set to a low level, such as $E^* = 10^{-7}$. But the converging process still needs millions of trials during the reconstruction. As for each temperature level that approaches the final, the objective function of the system should be calculated to determine whether the trail is accepted or not. It is significant to find a way to calculate the objective function of the system with high efficiency. And this would reduce the complexity and time for the reconstruction process.

Instead of calculating the objective function of the whole system which is to evaluate by performing a transformation on $\boldsymbol{M^*}$ to get $\boldsymbol{D^*}$, a calculation method is developed to reduce the complexity of the calculation. As only a small portion of the system is changed, only differences between $\boldsymbol{M_{old}}$ and $\boldsymbol{M_{new}}$ are obtained to calculate the objective function difference between $\boldsymbol{D_{old}}$ and $\boldsymbol{D_{new}}$. Practically, only the objective function that associate with the moving node in the ECM network is calculated in both old and new trails. This method will greatly reduce the calculation established in the reconstruction process and improve the efficiency of the convergence.

*Figure 2.8(a)* and *Figure 2.8(b)* shows some critical parameters change during the reconstruction process. The change of the objective function and acceptance rate in each stage are shown. At first, the temperature reduced fast so that the reconstructed system would quickly fit into a valley, shown in *Figure 2.7*. Then, the temperature will be reduced gradually. As a result, the objective function will be reduced to fit the local minimum of the valley.

E as the objective function of the reconstructed system also displays in *Figure 2.8(a)*. The objective function falls quickly in the first several stages which indicate that the system has approached the comparable level of local maximums of the valleys shown in *Figure 2.7*. And then, the speed of the decreasing of the objective function slows down as it was affected by the high acceptance rate. The high acceptance rate gives a chance for the up-hill objective function change. This would increase the chance for the system to reduce the objective function possibly approach to the global minimum. At last, as the temperature reduces to a relatively low level, it is difficult for the objective function to go up-hill. The objective function will finally reduce to the local minimum of the valley.

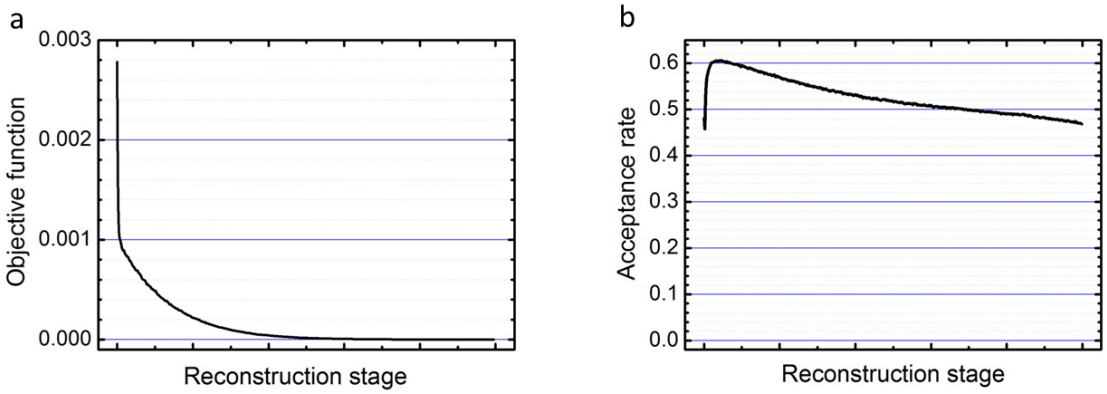


*Figure 2.8 The objective function and average acceptance rate change during the stochastic optimization of reconstruction; the stages represent the process of the reconstruction. (a) Objective function reduces during the reconstruction process; (b) acceptance rate varies in different stages.*

### 2.3 Reconstruction of heterogeneous collagen-based ECM

Now, we already knew how to reconstruct collagen-based ECM homogeneously, which means the topological and physical properties are homogeneous in all the direction. But in most situations, the micro-conditions of the cell in ECM are not homogeneous, such as stroma of breast tumor includes both remodeled collagens as well as dense basal membranes as we discussed in Introduction [70]. So we need to reconstruct heterogeneous ECM network as a basis to build up a model for tumor cell micro-mechanical analysis. In order to reconstruct heterogeneous collagen-based ECM, we manipulate one (or more) set of geometrical information that defines the network. That means one (or more) target dataset is altered by establishing a corresponding target dataset that represents a heterogeneous network. For the homogeneous network, all the target datasets are identical at different spatial areas of the network. For the heterogeneous network, one (or more) target dataset varies from different spatial areas.

When all the geometrical information as duplicated as the one extracted from the experimental built ECM network, the target of the reconstructed network would share the very same geometrical and mechanical properties. And the biological properties related to its mechanical characteristics should also be reproduced.

But practically, it is hard to build a collagen-based ECM network that would fit all the requirements, especially when building up a heterogeneous network that shares the same geometry and mechanical properties *in vitro*. That is because of the growth of the collagen is affected by all kinds of factors such as the concentration of the monomer of collagen, growth temperature, exchange of energy and substance while growing, the influence from the organism and organic matter, and *etc.*. As a result, it is difficult to reproduce ECM network experimentally which shares the same properties of the designed network. Thus, it is impossible to gain geometrical information $\boldsymbol{M}$ and original datasets $\boldsymbol{D}$ of the heterogeneous ECM network from the experiments.

Here in this project, the topologic dataset that represents as the target network is modified from the original network dataset gained from the homogeneous network. The orientation of the

fiber was chosen as a representative variable dataset from area to area in the network. In particular, the identical distribution of fiber orientation in a different part of the system is replaced by an elaborated distribution. Only the target distribution of fiber in the reconstructed network is altered with other dataset and parameters remain the same as the ones in the experimentally-gained homogeneous ECM network.

Besides, we could also manipulate the orientation of the fibers so that the fibers in the reconstructed network will represent different orientation compare with the original one. The basic idea is to substitute the original orientation of the fibers ***S*** with a manipulated ***S'*** of the dataset ***D***. Meanwhile, the other elements in the dataset ***D*** remain the same. In that way, a network with geometrical information ***M'*** will be reconstructed with all the other properties remain the same but the fiber orientation.

*Figure 2.9* shows a reconstructed network with all the fiber oriented parallel to the z-axis. *Figure 2.10* shows the comparison between distributions of target dataset and reconstructed dataset with homogeneously distributed cosine equals to 1. We could observe that in *Figure 2.10(a)*, the valence distributions match very well which indicated that the overall concentration of the nodes and fibers remain the same. The concentration of the collagen in the reconstructed network matches the same value in the original network. In *Figure 2.10(b)*, the difference between length distribution of reconstructed and the one of original is negligible.

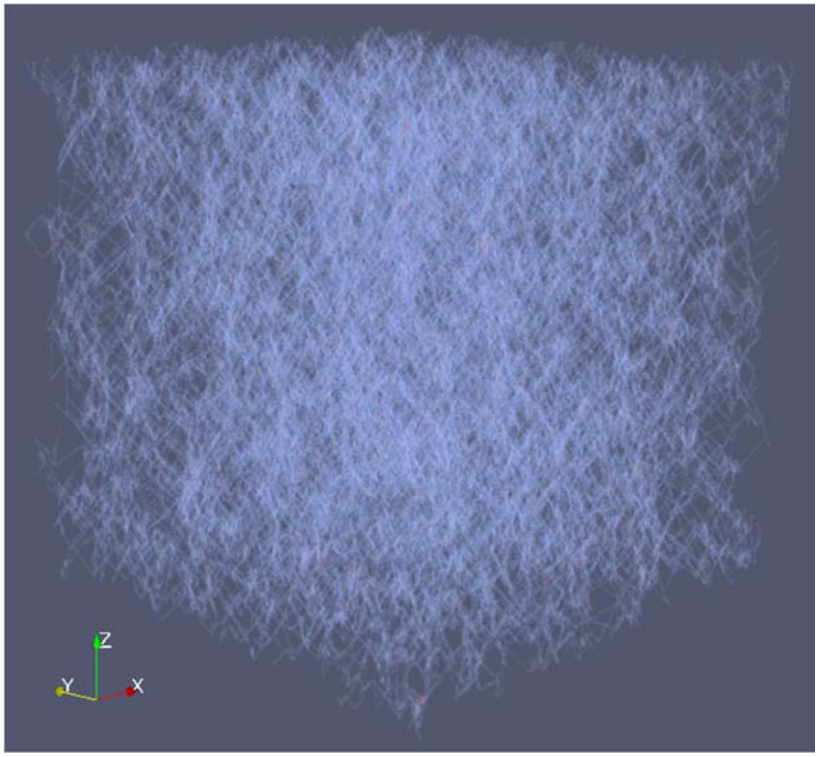


*Figure 2.9 A collagen-based ECM network reconstructed with homogeneous orientation of fiber parallel to z-axis*

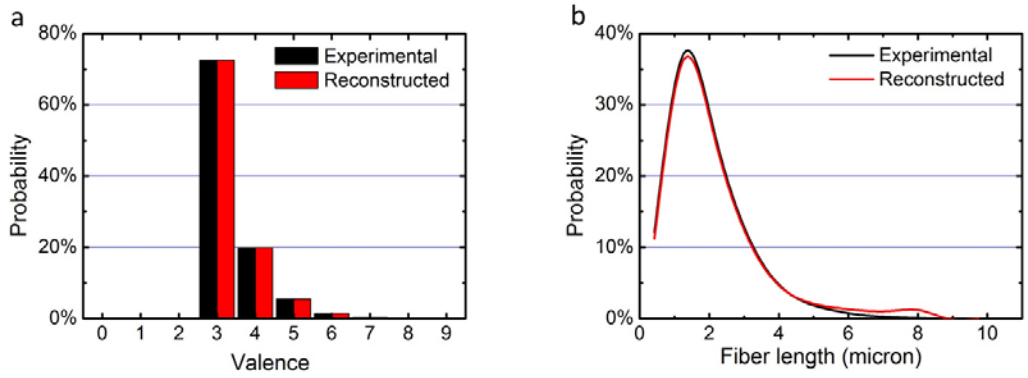


*Figure 2.10 The comparison between distributions of target dataset and reconstructed dataset with homogeneously distributed direction cosine equals to 1; (a) the valence distribution; (b) the length distribution*

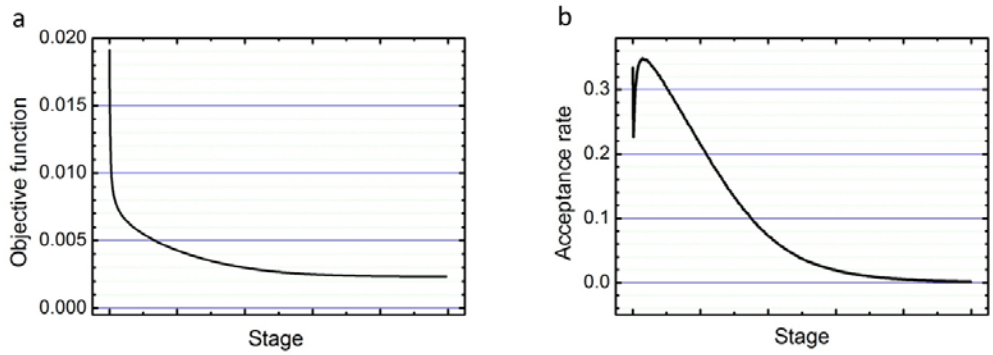


*Figure 2.11 The temperature, objective function and average acceptance rate change during the stochastic optimization of reconstruction of the network with cosine homogeneously distributed; (a) Objective function converges during the reconstruction process; (b) acceptance rate changes in different stages.*

The above reconstructions show the feasibility of the method. The aim of this project is to establish a reconstruction method to build up a heterogeneous collagen-based ECM network. Heterogeneity includes a wide aspect of differences in kinds, such as inconsistency of distribution of nodes, the variability of the distribution of fiber orientation in the network and *etc.*. Here in this project, we select the distribution of fiber orientation as a representative to build a heterogeneous network with different orientation of fiber from area to area.

A collagen-based ECM network with heterogeneous fiber orientation is constructed as shown in *Figure 2.12*. The reconstructed area has been divided into two areas: The upper area which occupies 70% of the volume will allow fibers have an orientation parallel to z-axis while the lower area occupies 30% of the volume will have fibers randomly oriented.

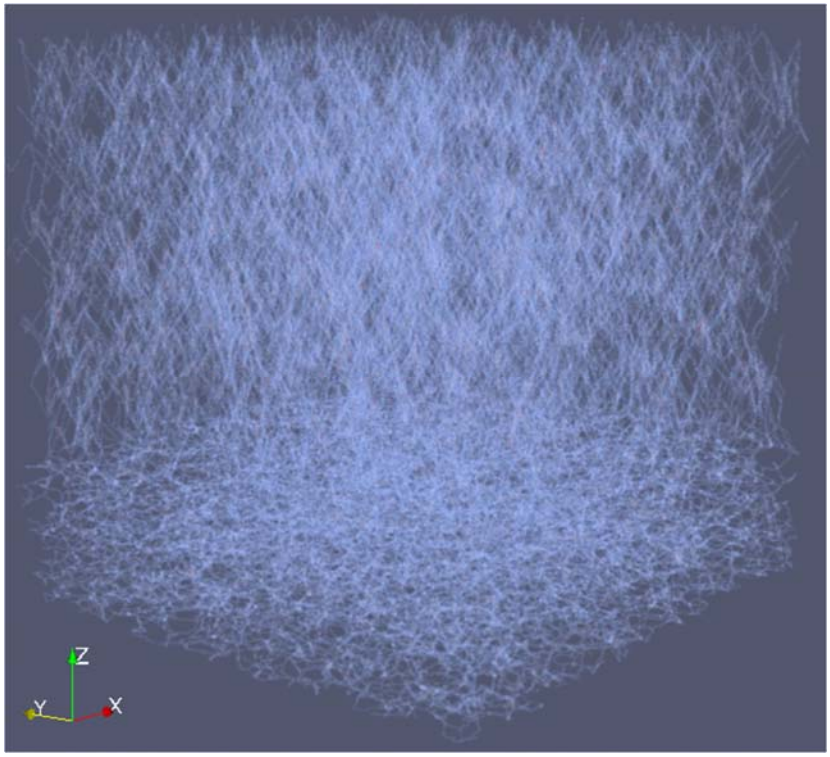


*Figure 2.12 A collagen-based ECM network reconstructed with heterogeneous orientation of fiber parallel to z-axis*

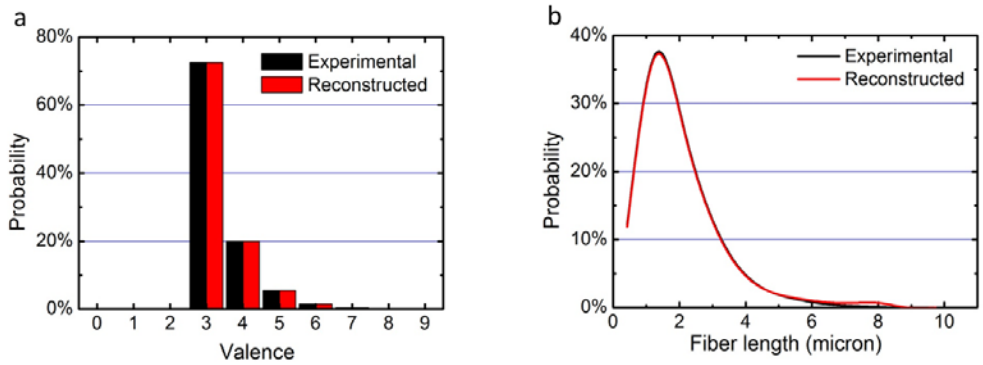


*Figure 2.13 The comparison between distributions of target dataset and reconstructed dataset with heterogeneously distributed cosine; (a) the valence distribution; (b) the length distribution*

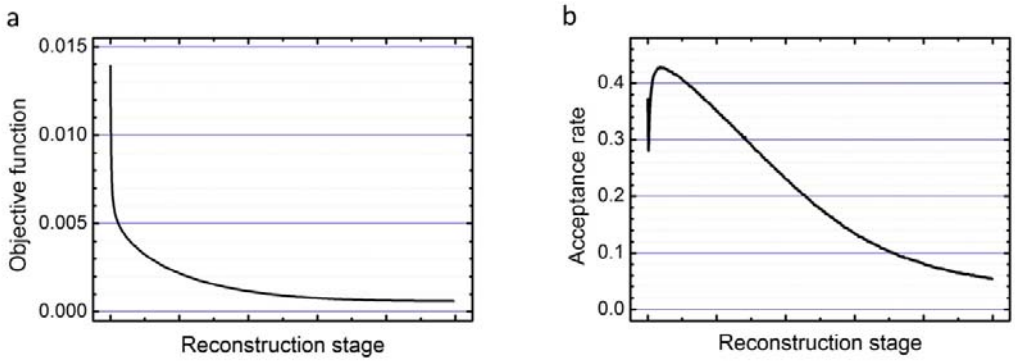


*Figure 2.14 The temperature, objective function and accumulated acceptance rate change during the stochastic optimization of reconstruction of the network with cosine heterogeneously distributed*

*Figure 2.13* shows the statistics comparisons between the valence distribution and fiber length distribution statistics that is set as the target (original) of the reconstruction and the corresponding ones. It is clearly noted that the valence distribution of the reconstructed network fit the target statistic very well. Meanwhile, despite a negligible mismatching of the fiber length distribution at the higher end, the two curves fit very well.

*Figure 2.14* shows the parameters change during the reconstruction process. The changing tendency of virtual temperature, objective function and direction cosine during the process remain the same compared with the ones shown in the reconstruction of homogeneous ECM network.

**2.4 Micro-mechanical model of fiber in collagen-based ECM network**

In this section, we briefly describe our micromechanical model for force analysis in collagen-based ECM. The ensuing discussion follows closely to that in reference [21], to which the interested readers are referred to for more details. Specifically, shown as in *Figure 2.15*, we employ a nonlinear elastic model recently developed by Steinwachs *et al.* to characterize the

stretching and compression of a collagen fiber [97]. In particular, upon stretching, a fiber first enters a linear elastic regime, which is followed by a strong strain-hardening regime once the elongation is larger than a prescribed threshold. Upon compression, we consider the fiber immediately buckles and thus, possesses a much smaller compression modulus.

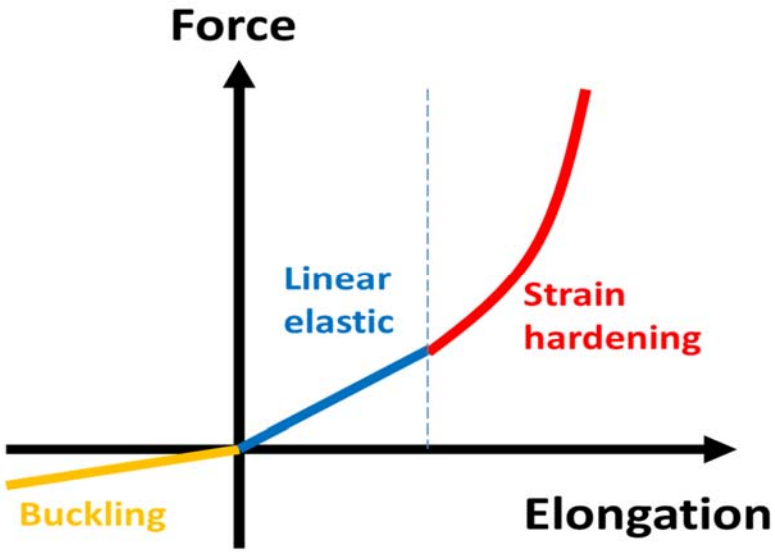


*Figure 2.15 Schematic illustration of the nonlinear micromechanical model of an ECM fiber, which buckles upon compression and exhibits strain-hardening upon stretching.*

The elongation stiffness $k$ of the fiber is thus given by

$$k = \begin{cases} \rho EA, & \lambda < 0 \\ EA, & 0 < \lambda < \lambda_s \\ EA exp(\frac{\lambda - \lambda_s}{\lambda_0}), & \lambda > \lambda_s \end{cases}$$

Where $E$ and $A$ are, respectively, the Young's modulus and cross-sectional area of the fiber bundle, and we use $EA = 8 \times 10^{-7}$ N [45]; $\lambda = \delta l / l$ is elongation strain, and $\lambda_s = 0.02$ and $\lambda_0 = 0.05$ are parameters for the strain-hardening model [98]; $\rho \in [0,1)$ describes the effects of buckling [74]. We model an embedded polarized cell as an ellipsoid with semiaxis $R_a = R_b < R_c$ respectively along the $x$, $y$, and $z$-axis, centered at a prescribed location in the network. This simple shape is our first

attempt to model a migrating cell which typically develops a polarized morphology [66]. The contraction of the cell pulls the nodes residing within a cone region defined by the polar angle $\theta$ in the cell towards the cell center, which is modeled by an affine transformation with a contraction ratio $\gamma$, see *Figure 2.16*. In the subsequent simulations we use $\theta = \pi/2$ and $\gamma = 0.93$.

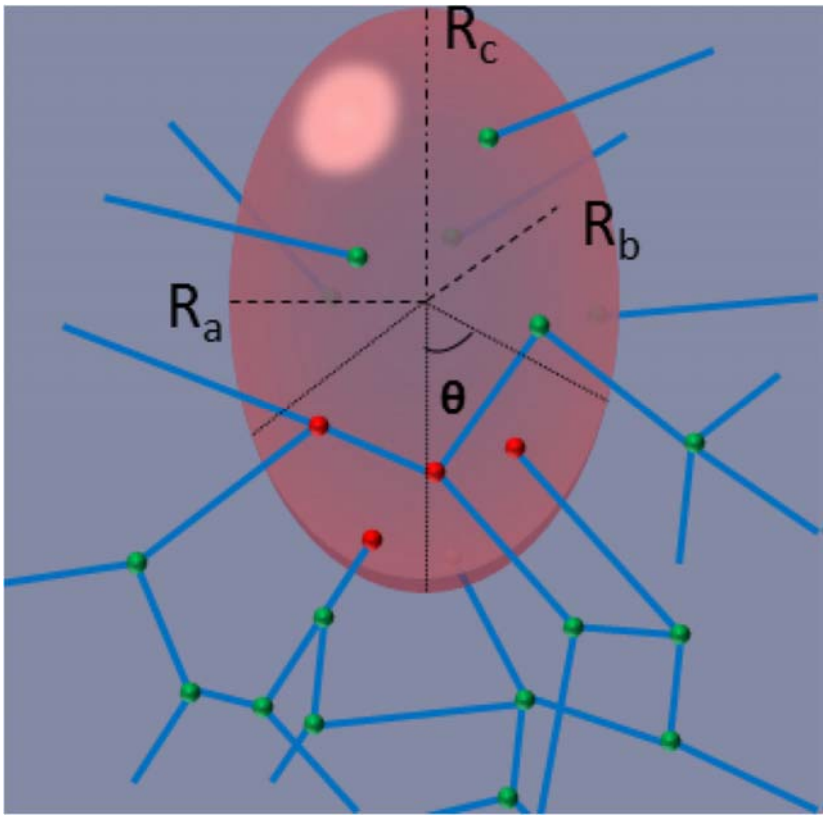


*Figure 2.16 Schematic illustration of the polarized contraction of an ellipsoidal cell embedded in the collagen network. The nodes within a cone region defined by the polar angle θ are pulled towards the cell center by an affine transformation.*

After cell contraction, a force-based relaxation method is employed to obtain the force-equilibrium network configuration and resolve the forces on each fiber. Specifically, at each iteration, a node *i* is displaced along the direction of the net force on this node, with the magnitude of the displacement proportional to the magnitude of the force $\mathbf{F}^i$, i.e.,

$$\delta_i = \mu \left| \mathbf{F}^i \right|$$

Where $\delta_i$ is the magnitude of the displacement and $\mu$ is an effective mobility parameter. The upper bound of $\mu$ is chosen such that the maximal individual displacement is ~1/100 of the average fiber length. Once the positions of all nodes are updated, the new net force of each node is computed, which determines the nodal displacement. This process is repeated until the maximal net force on a node is smaller than a prescribed tolerance (e.g., $1 \times 10^{-10}$ N).

### 2.5 Validation of the method by micro-mechanical analysis ECM with deformed tumor cells

In order to validate the method that could reconstruct the homogeneous network, a cell is introduced to the reconstructed system to check if the mechanical property of the reconstructed network would fit the prophetic results. A cell with ellipsoidal shape is embedded at the center of the reconstructed network system to perform asymmetry contraction to the fiber attached. We noted that in actual *in vivo* cellularized ECM systems, round-shaped cells are rarely found. But the simple model with an ideal geometry of cell can still provide useful insights. For example, the ellipsoidal symmetry allows carrying out radial mechanical influence distributed over its axis, while the force field generated by the contracting cell can be compared to the continuum mechanics predictions. The effects of elongation of cell shape on the resulting force network have been systematically investigated using 2D random network models [61]. Besides, the cell can occur as a near-ellipsoidal-shape when certain environmental parameter matches. For example, *Figure 2.17* shows a NIH 3T3 cell cultured in 3D COL-I gel. This particular cell could be compared with our simulation using ellipsoidal cell [21].

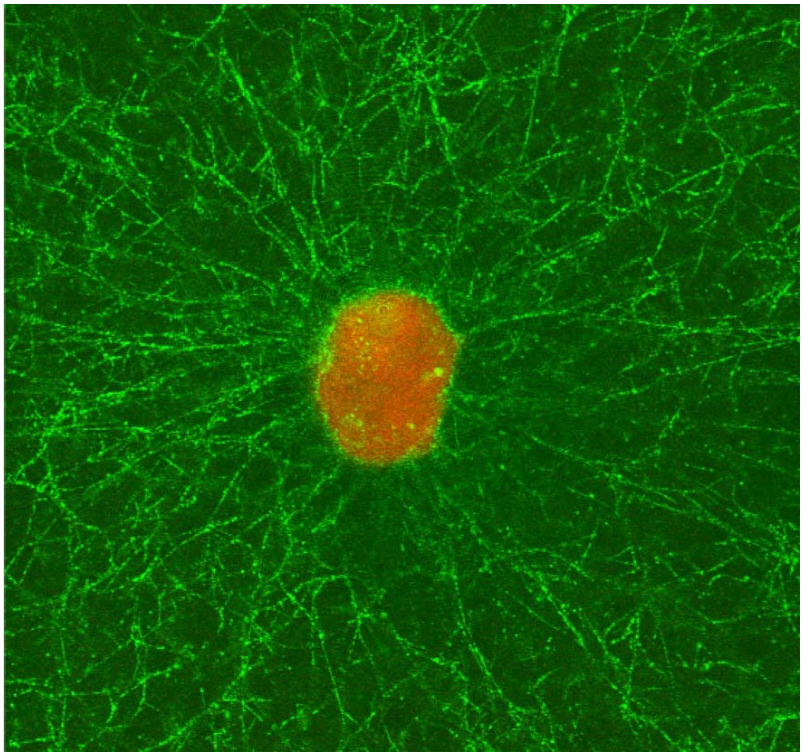

*Figure 2.17 A contracting NIH 3T3 cell with an almost spherical morphology cultured in collagen I gel. Linear chain-like structures of collagen fibers emitting from the cell can be clearly observed [21].*

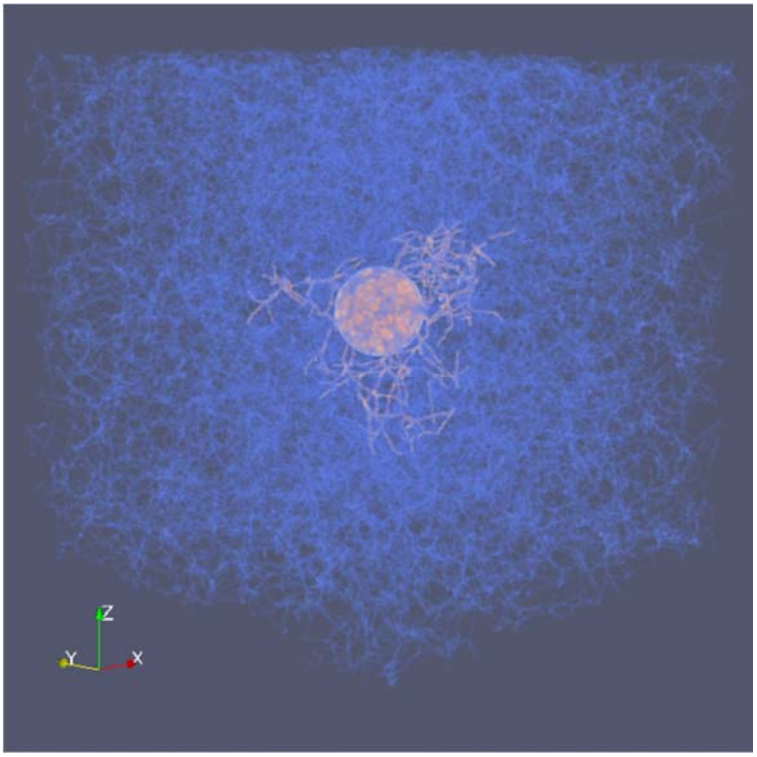


*Figure 2.18 A collagen-based ECM network reconstructed homogeneously, with an ellipsoidal cell contracting at center; fibers highlighted in red undertake critical mechanical strength*

We could observe from *Figure 2.18*. The fibers (shown in blue and red) are built from the reconstruction. The ellipsoidal cell (shown in pink) in the middle contracts evenly. The fibers which highlighted in red bear the critical mechanical strength. Only the top 1% of the fiber is highlighted. It is shown that the highlighted fibers diverged from the evenly contracted cell radiate into the cell's neighbor. The highlighted fibers connected head-to-tail are considered as force chains. Along with this force chains, the cell exerts mechanical power into its neighbor ECM.

We can observe that the force chains exert from the cell are evenly distributed around the cell. Because of the disordered nature of the reconstruction, the force chains propagate heterogeneously in different spatial directions. The distribution pattern is very like the one shown in *Figure 2.17*, which is a microscopic image taken from an experiment *in vitro*. Thus, we can mimic the ECM that grows in a practical experiment using our model.

The effects of ECM microstructure on force chain propagation patterns are also studied. *Figure 2.19* shows how the mechanical force chains distribute when an ellipsoidal cell contract in the same pattern at the center of the network with different fiber orientations. The original semi-axes of the ellipsoidal cell are 6.84 μm, 6.84 μm, 10.26 μm, respectively. All the cells contract 7% in volume at its Z-end, which means the nodes associated with the z minus hemisphere of the cell displaces toward the cell center. All the fibers highlighted following the same threshold which is $1.0\times10^{-7}$. *Figure 2.19(a)* shows the contraction of cell embedded in a homogeneously reconstructed network with randomly orientated fibers. *Figure 2.19(b)* shows the cell contracts with the same pattern in the ECM network that has all the fiber homogeneously aligned with the z-axis. *Figure 2.19(c)* shows the propagation of mechanical force when cell contracts in a heterogeneously reconstructed network we discussed. And *Figure 2.19(d), Figure 2.19(e) and Figure 2.19(f)* are the observation at a different aspect of the network shown in *Figure 2.19(a), Figure 2.19(b) and Figure 2.19(c)*, respectively. Compare with all the mechanical force chains propagation patterns, it can be easily noted that the least amount of fibers are highlighted in ECM that has randomly orientated fibers. This indicates that the force chain will propagate the least distance. Also, the forces chain will propagate further if the orientation of the fibers is aligned with the contraction direction. Compare with *Figure 2.19(a) and Figure 2.19(c)*, the force chains generated by the contraction of the cell in the network (a) only propagate no longer than semi-axis of the cell, while in the network (b), the forces chain reach as far as 3 times as the semi-axis propagate along z-direction.

Besides, when the propagation of the force chains penetrate into an area with a lower order of alignment of the fibers, such as in network present in *Figure 2.19(c) and Figure 2.19(f)*, the propagation will be held back from propagating along its former direction. Instead, the propagation of the force chains will be deflected homogeneously into the respective area with fiber orientated randomly.

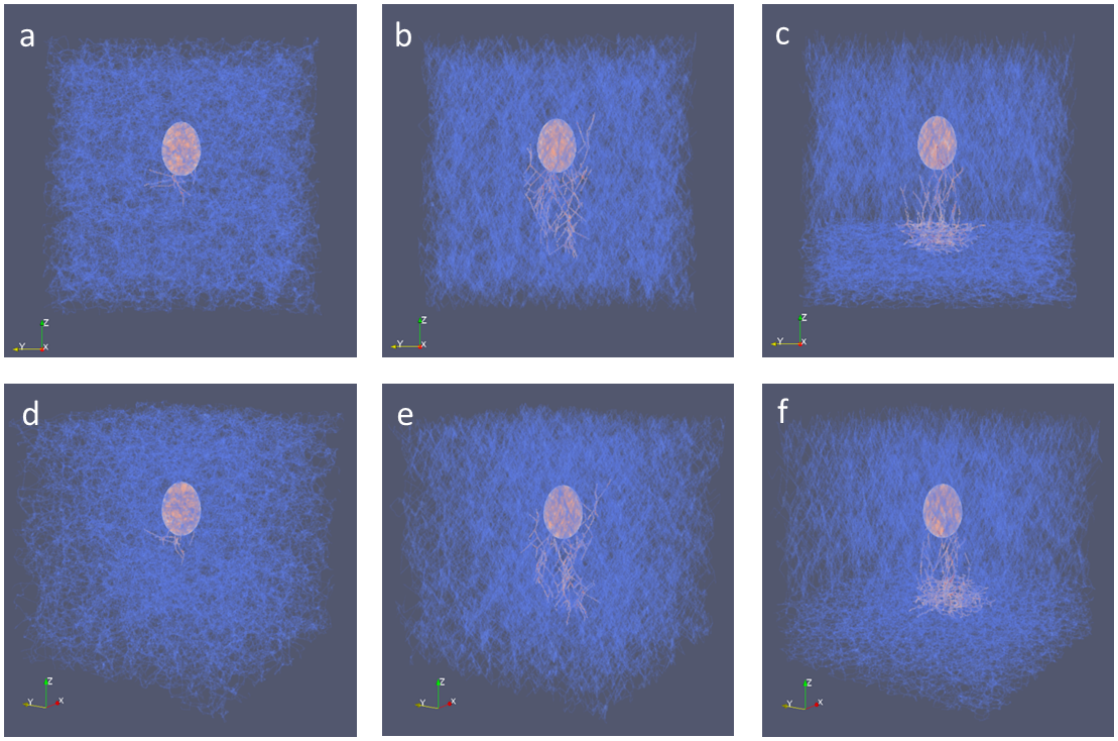


*Figure 2.19 Different reconstructed collagen-based ECM networks with an ellipsoidal cell contracting in the same pattern at center; fibers highlighted in red undertake critical mechanical strength; (a) & (d): ECM network reconstructed homogeneously; (b) & (e): ECM network reconstructed homogeneously with the fiber parallel to z-axis; (c) & (f): ECM network reconstructed heterogeneously, with fibers in 30% of the area has no preference of orientation and 70% if the area align with z-axis*

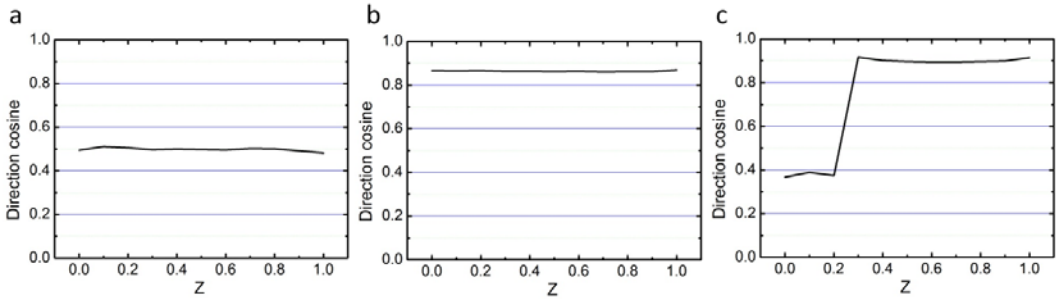


*Figure 2.20 Orientation of fibers at different areas divided along z-direction. The descriptor of the orientation is set as the direction cosine of angle between fiber and z-axis; (a): ECM network reconstructed homogeneously without control of fiber orientation; (b): ECM network reconstructed homogeneously with the fibers align with z-axis; (c): ECM network reconstructed heterogeneously, with fibers in 30% of the area has no preference of orientation and 70% if the area align with z-axis*

This could explain that during the cluster migration of the breast cancer cells, the cell could easily penetrate into dense basal membrane (represent as randomly orientated fibers at lower area in *Figure 2.19(c) and Figure 2.19(f)* leaving from adjacent primary tumor area (represent as strongly oriented fibers at upper area in *Figure 2.19(c) and Figure 2.19(f)*.

The fibers in the primary tumor area have been modified for penetration with all the fibers orientated perpendicular to the invasion plane with a relatively low density of fibers. Moreover, the force chains can propagate further along the aligned fibers. As a result, the force chains generated even by a relatively distanced contracting cell would penetrate into the dense membrane. Thus, the randomly orientated fibers adjacent to boundary will be remolded into ones with an orientation parallel to the propagation direction of force chain. This will help the tumor cell enlarge the area with orientated fibers, in which the migrating cells will have less obstruction worming its way into the dense membrane.

Without the help of the linear orientated fiber, the penetration to the dense membrane will be impossible, shown in *Figure 2.19(a) and Figure 2.19(d)*. With the same contraction applied to the exact cell, the force chain will not last as long as the length of its semi-axis.

We have established a model for mechanical analysis of the local environment of invasive tumor cell based on the stochastic reconstruction of collagen-based ECM. After extracting topological and geometrical information from limited confocal microscopy images, the collagen-based ECM is reconstructed as an optimization problem, in which the objective function is the squared sum of the difference between the experimentally measured original and the corresponding simulated network statistics. The simulated annealing method is subsequently used for randomly perturbing the random initial network microstructure to minimize the objective function.

To validate the model, a deformed schematic virtual cell is embedded into ECM to show the mechanical response of ECM as well as orientated force propagation in ECM. A nonlinear elastic model is employed to characterize the mechanical behavior of individual fiber segments. The fibers which sustain critical mechanical force are highlighted. The radical pattern of the fibers that in the vicinity of the contractile cell match the one shows in the microscopic image. Thus, the model can reproduce the mechanical-induced fiber orientation and can be used as a tool to analyze the force network of contractile cells.

Furthermore, some experimentally measured original statistics are manipulated as the target statistics to reconstruct heterogeneous ECM which could reproduce more circumstances of micromechanical cell-ECM interactions. In specific, a heterogeneous ECM network is reconstructed with partially modified statistics, which reproduce the environment where the breast cancer cells penetrate the dense basal membranes to enter the circulation system.

The force chains generated by the modeled contracting ellipsoidal cell spread out heterogeneously give an explanation of the penetration of the breast cancer cell. The force chains could reach out to a further distance while an orientated bridge of fiber occurs between the contracting cell and basal membranes.

### 2.6 Micro-mechanical analysis with multiple deformed tumor cells

Besides, the influence of multiple cells in heterogeneous collagen-based ECM network is also considered. A micro-mechanical analysis with multiple deformed tumor cells is conducted in heterogeneous network reconstructed, as shown in *Figure 2.21.*

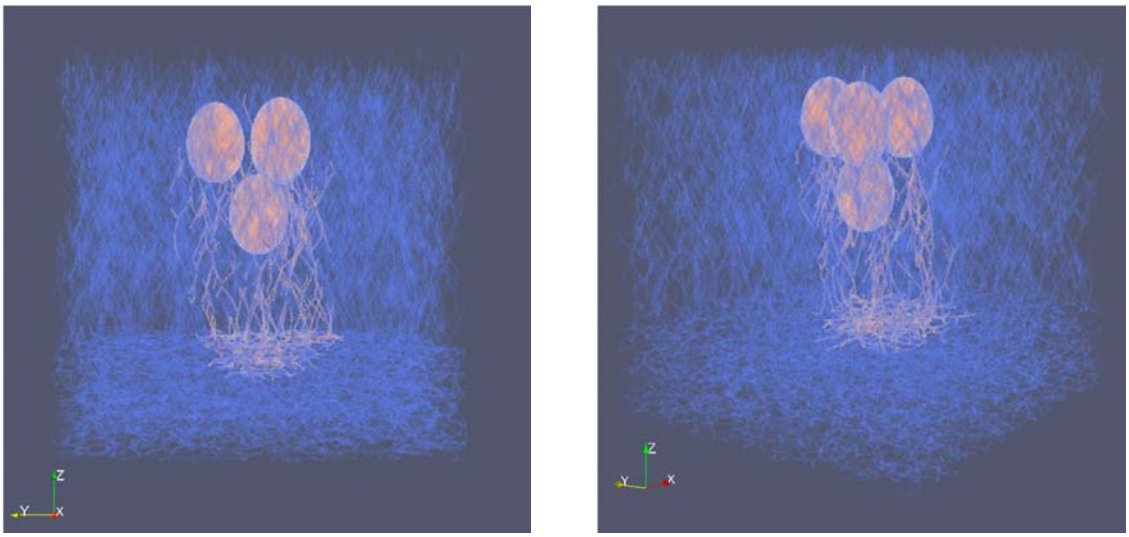

*Figure 2.21 Micro-mechanical analysis of reconstructed collagen-based ECM networks with multiple ellipsoidal cells contracting in the same pattern; fibers highlighted in red undertake critical mechanical strength.*

The heterogeneous ECM network here is a mimic of the condition of a migrating tumor cell at the boundary of collagen region (upper part) attached to a layer of dense Matrigel. For the breast cancer cell we discussed in the Introduction section after the tumor cell penetrates into the Matrigel layer, the tumor cell will be easily released to the circulatory system, in another word, the metastasis of the tumor happens.

In *Figure 2.21*, we can observe that compare with force chain exert by a single cell, the multiple cells exerted force chain will form a bundle, which is thicker than single cell exerted chains. And the force chain bundle will affect even a larger area in a randomly oriented part, which is the

Matrigel layer. Due to the contact guidance, the cell tends to move along those force bundles that align with the orientation of fiber in ECM. So we can draw a conclusion that the migrating tumor cells will exert force bundle to modify the neighboring micro-environment to the benefit of invasion. Thus, a *migration highway* is formed for the cell to move from the primary tumor area to the basal membrane. So now we can explain how the heterogeneity of microstructure of ECM will mechanically accommodate the migration of tumor cells.

### 2.7 Collective cell invasion behavior, an example of micro-mechanical remodeling of ECM by geometry controlled tumor organoids

In another point of view of the Collective invasion of cancer cells, we consider the cell-cell adhesion leads to group invasion as cell clusters [98,99]. Strands of cells may follow each other along micro-tracks created by leader cells [100,101]. Communications mediated by diffusive factors have also been shown to coordinate the collective motility of tumor cells by establishing leader-follower phenotypes [102].

So we use a model to demonstrate that physical interactions between cells and ECM support coordinated dissemination of cells from tumor organoids, in order to gain further insights on how collective ECM remodeling modulates the collective cancer invasion. We devised a multi-scale computational model that takes into account the fibrous microstructure of the ECM [45], ECM mechanics [97], as well as cell motility directed by contact guidance cues [70].

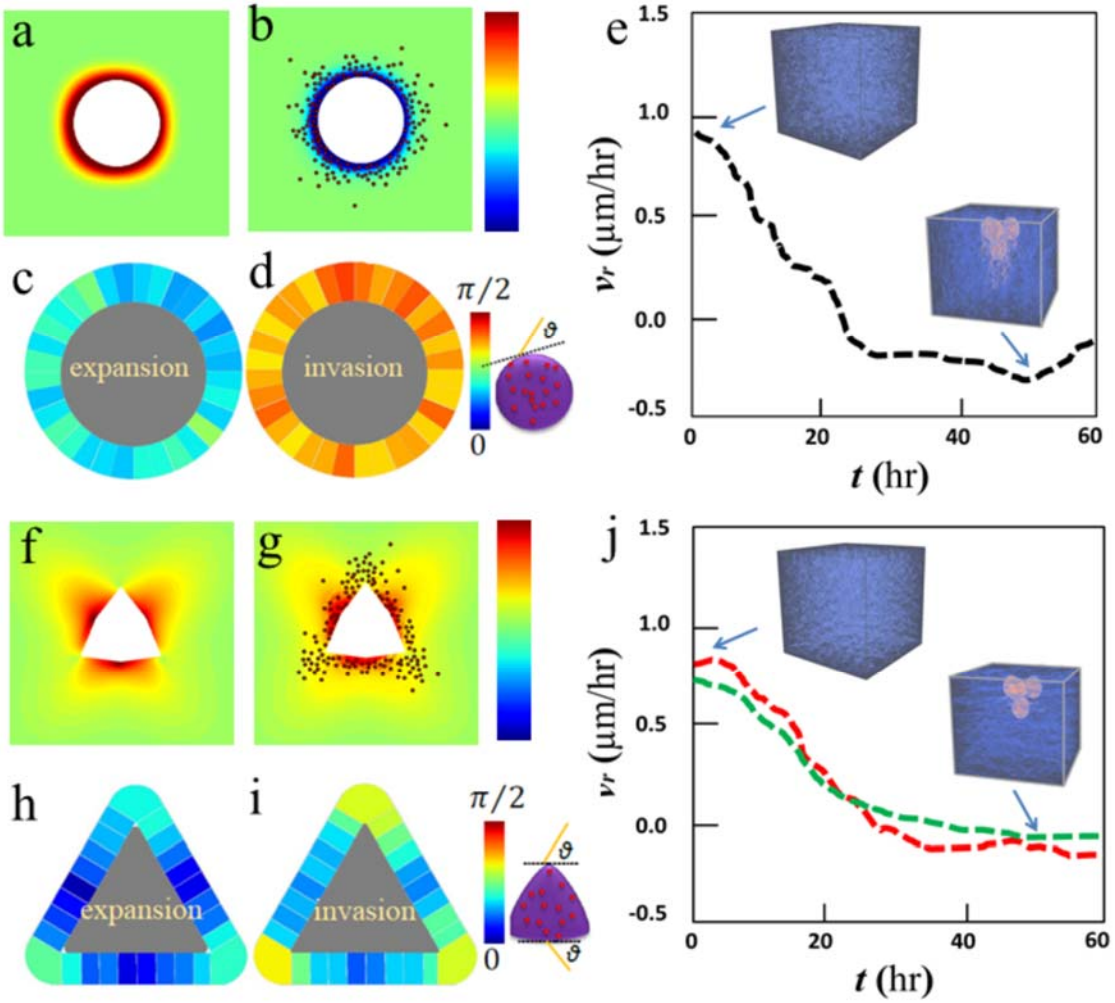
a
b
c
d
expansion
invasion
π/2
ϑ
0
e
1.5
1.0
0.5
0.0
-0.5
0
20
40
60
$v_r$ (μm/hr)
$t$ (hr)
f
g
h
i
expansion
invasion
π/2
ϑ
ϑ
0
j
1.5
1.0
0.5
0.0
-0.5
0
20
40
60
$v_r$ (μm/hr)
$t$ (hr)

*Figure 2.22 Simulated ECM remodeling by circular and triangular tumor organoids. (a) and (f) respectively show the magnitudes of ECM displacement fields due to the expansion of circular and triangular organoids. (b) and (g) respectively show the magnitudes of ECM displacement fields after 50 hours of invasion by circular and triangular organoids. Dots represent simulated cell locations. (e) and (j) respectively show the time-dependent ECM deformation along the radial direction (i.e., radial velocity) sampled near the organoids at the locations corresponding to the experimental cases. The insets respectively show the local fibrous ECM configuration (in a cubic representative volume with the linear size of 100 μm) during the expansion and invasion phase, where the fibers carrying large tensile stress due to cellular traction forces are highlighted. (c) and (h) respectively show the orientation of ECM fibers near the organoids after the expansion phase, measured as the angle with respect to the local tangential direction of the tumor boundary. We sample 100 μm3 volume elements next to the organoids to obtain the average angle. (d) and (i) show the ECM fiber orientation after 50 hours of the invasion.*

Based on the experimental observations, we consider the dissemination of tumor organoids to start from an expansion phase, where cells spread and push out the ECM. This is followed by an invasion phase, where cells pull in the ECM and migrate. We model tumor cells as polarized active particles with coupled force generation and locomotion [70] (see SI for details). Cells deform the ECM fibers in their vicinity, which in turn alters the migration and polarization of the cells. Explicitly accounting for the reciprocal interactions between cells and ECM allows us to investigate the collective migration regulated by the non-local mechanical dialogues among the cells mediated by the ECM.

We first employ the computational model to calculate the remodeling of the ECM regions surrounding the tumor organoid (see SI for details). *Figure 2.22(a)* and *Figure 2.22(f)* respectively show the compressive displacement fields in the ECM due to the expansion of the tumor organoids with circular and triangular shapes [29]. The magnitude of displacement falls off as $1/r^6$ from the center of the organoids. The expansion phase is followed by the invasion phase, where individual cells interact with the ECM while migrating away from the original organoid. *Figure 2.22(b)* and *Figure 2.22(g)* are snapshots of the ECM deformation field at 50 hours. In particular, the insets in 2c and j show the simulated ECM microstructure in cubic representative volumes with a linear size of 100 μm. It is clear that the ECM fibers in the vicinity of the organoid are re-oriented due to the forces generated by the cells, which also redistribute the mechanical stress in the ECM. *Figure 2.22(e)* and *Figure 2.22(j)* are the radial velocity of the ECM measured near the organoid boundary. These results agree with the key experimental observation, i.e., the contractile deformation is much more pronounced near circular tumors compared with triangular tumors.

To better reveal the mechanical remodeling of the ECM, we have calculated the average orientation of the ECM fibers with respect to the tangential direction of the tumor boundaries (*Figure 2.22(c)*, *Figure 2.22(d)*, *Figure 2.22(h)* and *Figure 2.22(i)*). During the expansion phase, organoids push the fibers to be aligned parallel to the tumor boundary, which bias the cell polarization accordingly. Later on, the pulling forces from the cells reorient the fibers. For circular tumors, the collective cellular traction force is sufficient to align the ECM fibers radially shown in *Figure 2.22(d)*,

contributing to the accelerated the dissemination. In contrast, the fibers remain tangentially aligned along the flat edges of the triangular tumors, see *Figure 2.22(h)* and *Figure 2.22(i)*.

Our simulations show that the circular tumors possess a larger invasion depth compared with the triangular tumors (see SI), which is consistent with the experimental observations. To further explore the mechanisms behind the geometry-dependent collective migration, we modified the simulation parameters to steer the cell-ECM interactions. We find that when the cell polarization and ECM fiber orientations are uncorrelated, the invasion depth of circular tumors drastically reduces (see SI). This is consistent with the experimental results which showed that eliminating contact guidance diminished the advantage of circular tumors in dissemination (see SI). We also find that reducing the cellular traction forces leads to weaker ECM remodeling, and thus weaker dependence of tumor invasion dynamics on the organoid geometry (see SI for details).

Also, the simulated model is compared with an experiment designed. And our simulation match with the results from the experiments very well. To study the 3D collective invasion of cancer cells, tumor organoid models created with DIGME technique [29] is used. Each organoid consists of approximately 1000 GFP-labeled MDA-MB-231 cells molded into various shapes in 3D type-I collagen ECM (Methods). Confocal imaging starts immediately after the gelation process completes (marked as time zero).

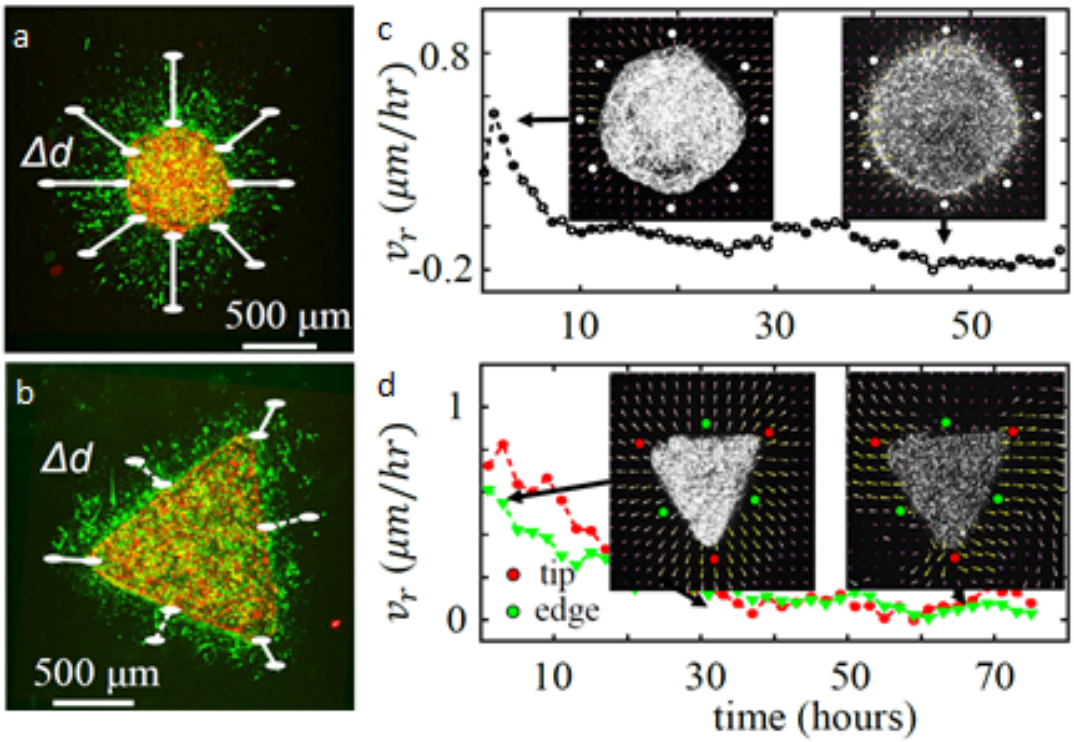


*Figure 2.23 Geometry controls tumor organoid invasiveness and ECM remodeling. (a-b) Tumor organoid morphology shown by maximum projection at day 0 (red) and day 10 (green). For a circular tumor the invasion depth Δd is measured along eight equally spaced angles (a). For a triangular tumor Δd is measured along tip and edge directions separately (b). (c-d) The average radial velocity of the ECM deformation near expanding tumors. In (c) the velocity is averaged over the 8 dotted locations shown in the inset. In (d) the velocity is averaged over the dotted locations along the edge and tip directions respectively. Insets in (c-d) show the net deformation of the ECM at two time points (black arrows).*

First, tumors of two different cross-sectional geometries, circular and triangular, are involved in the experiment. In particular, we measure the invasion depths Δd as the distance between the outer boundaries of the tumors at day 0 and day 10 as shown in *Figure 2.23(a)* and *Figure 2.23(b)*. The circular tumors disseminate rapidly, with the mean invasion depth to be more than 500 μm. The triangular tumors, on the other hand, disseminate much slower. The invasion depths measured in the edge and tip directions are both around 200 μm.

The cells in the organoids are harvested from the same subculture, and the invasion assays are maintained in the same tissue culture conditions, it is very unlikely that circular tumors and triangular tumors consist of two distinct phenotypes. Ruling out single-cell sources, it suggests that the 3D invasion of a tumor organoid is a complex multicellular phenomenon, where cell-cell and cell-ECM interactions may play important roles. We first note that there are rarely any cell-cell adhesions during the invasion process due to the highly mesenchymal nature of MDA-MB-231 cells. For a disseminating tumor organoid, the micro-mechanical remodeling of the ECM could be even stronger due to additive effects. Therefore, we hypothesize that collective cell remodeling of the ECM renders the invasion of tumor organoids to depend on organoid geometry.

To test this hypothesis, we first examine if the ECM deformation caused by tumor-generated mechanical forces depends on tumor geometry. We embed 1 μm diameter fluorescently-labeled polystyrene particles in the collagen ECM and use particle image velocimetry (PIV) to quantify the ECM deformation field. *Figure 2.23(c)* and *Figure 2.23(d)* show the radial velocity vr of the ECM by averaging over symmetric locations (dotted points in the insets of *Figure 2.23(c)* and *Figure 2.23(d)*). A circular tumor first pushes out the ECM ($v_r > 0$) due to cell spreading upon seeding (leading to overall expansion of the organoid), then pulls in the ECM ($v_r < 0$) with their traction force. As a result, after 2 days the ECM shows net inward deformation while some of the cells have already been disseminated from the tumor (*Figure 2.23(c)* insets). On the other hand, we find that a triangular tumor mostly pushes out the ECM, albeit with a diminishing rate. As a result, the ECM surrounding the triangular tumor maintains a radially outward net deformation (*Figure 2.23(d)*).

These experimental results agree well with the predictions of our simulations. Here, we demonstrate a previously unrecognized mechanism of cell-cell interaction that coordinates multicellular dynamics. This mechanism does not require direct contact between cells such as cadherin-based adhesion [98,99] or contact inhibition [103,104], nor it relies on the cooperation of leader-follower phenotypes [100,101,105,106]. Instead, we show both experimentally and computationally that cells collectively apply forces to their ECM [29], which in turn provides mechanical cues to bias cell motility. Because collective force generation can be controlled by geometry, we find dissemination of cancer cells from tumor organoids are dependent on tumor geometry. Our results provide physical insights for processes in cancer biology and morphogenesis. Clinical studies have shown that collagen fibers aligned tangentially and normally to tumor boundary correspond to opposite prognosis [107,108]. While the origin of tumor-associated ECM misalignment is unclear, our results suggest that tumor geometry is an important contributing factor. On the other hand, mesenchymal cell migration is often considered as a single-cell process during development and diseases [109,110]. Our model system shows that underlying multicellular coordination may take place in the form of collective force generation and ECM remodeling. Together, we find that 3D collective cell migration may exploit the mechanical feedback between force-generating cells and reconfigurable ECM as an indirect yet effective channel of communication.

Finally, our results show that 3D migrating cells represent a distinct class of active particles which actively re-sculpture their microenvironment and respond to the cues generated by themselves and others. Future research is needed to systematically investigate the collective dynamics of such active particles as a route to understanding general living systems. We show both experimentally and computationally that the reconfigurability of ECM, as well as the force generation and force sensation of cancer cells, maintain a mechanical conversation between invading tumor cells in 3D tissue space. As a result, the collective invasion is coordinated by collective micromechanical remodeling of the ECM, which leads to organoid-geometry dependent dissemination of the tumor cells. Our results suggest that ECM-mediated physical interactions

between invasive cells may play a powerful role in determining the metastatic potential of malignant tumors.

### 2.8 iFEM for resolving cell-ECM micromechanical interaction

To better understand the cell-ECM micro-mechanical interactions, we also develop an inverse finite element method (iFEM) for accurately resolving the traction forces generated by a migrating cell in heterogeneous 3D ECM. Our formulation does not require any a priori knowledge of the boundary conditions, and simultaneously results in the distribution of the heterogeneous modulus values and stress field in the ECM, as well as the traction forces on the cell, given experimentally measured average modulus of the ECM. We first validate our procedure in artificial model cell-ECM systems, and then employ the procedure to compute the distribution of elastic modulus in a heterogeneous type-I collagen gel as well as the traction force on a rounded breast cancer cell in the gel, based on the deformation field data obtained via 3D reflectance force microscopy. We will briefly present the key results here and refer the readers to [111] for details.

We apply our iFEM to resolve traction forces on a rounded MDA-MB-231 breast cancer cell embedded in type-I collagen gel (ECM) with a collagen concentration of 2 mg/ml. This system is particularly selected since the contraction magnitude of the cell is relatively small, and the cell maintainns a rounded shape. In this case, it is reasonable to assume that linear elastic deformation dominates in the ECM and it serves as an ideal demonstration case for our general reconstruction procedure. The Poisson's ratio of ECM is set to be 0.33. We note that recent studies have shown that ECM can possess an unusual asymmetric Poisson's ratio due to fiber micro-buckling in case

of large deformation. Here, we still use the normal value, which is a good approximation for small linear deformations.

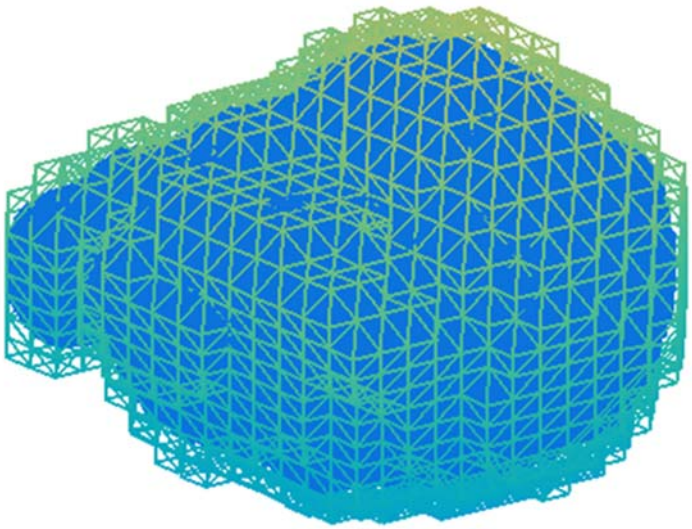

*Figure 2.24 The geometry of the MDA-MB-231 breast cancer cell embedded in the ECM and its surface mesh using tetrahedral elements.*

The morphology of the cell is obtained via confocal microscopy and the displacement field within the ECM region is obtained via 3D reflectance force microscopy. The reconstruction domain is a cubic box with linear sizes 355 $\mu m$ by 355 $\mu m$ by 355 $\mu m$ along each direction. The domain is meshed into 63 by 63 by 65 grids, on which the displacements are obtained. The total number of experimentally measured displacement points within the ECM region is 255405.

The reconstruction domain first meshes with linear tetrahedral elements and the available displacement data is mapped to the corresponding mesh grid points. Specifically, the mesh for ECM is generated as follows: first, we tessellate the entire system into tetrahedral elements including both the ECM region and the cell region. We then check each element and exclude those elements

which contain at least one node within the cell. The remaining ECM elements and the associated nodes are re-ordered and each is assigned with a new global element (node) index. The surface of the cell is approximated by an appropriate triangle tessellation compatible with the tetrahedral elements at the cell-ECM interface, see Fig. 2.24. The normal vector of each boundary facet, including the exterior boundary reconstruction domain and the cell-ECM interface is obtained for approximating boundary forces using the unknown modulus and smoothed boundary strain. We note that although generally, the use of tetrahedral elements for elasticity analysis would lead to artificially stiff deformations due their “locking” effects, our subsequent validation based on the evolution of cell morphology indicates the current mesh method and the tetrahedral elements work fine in our analysis.

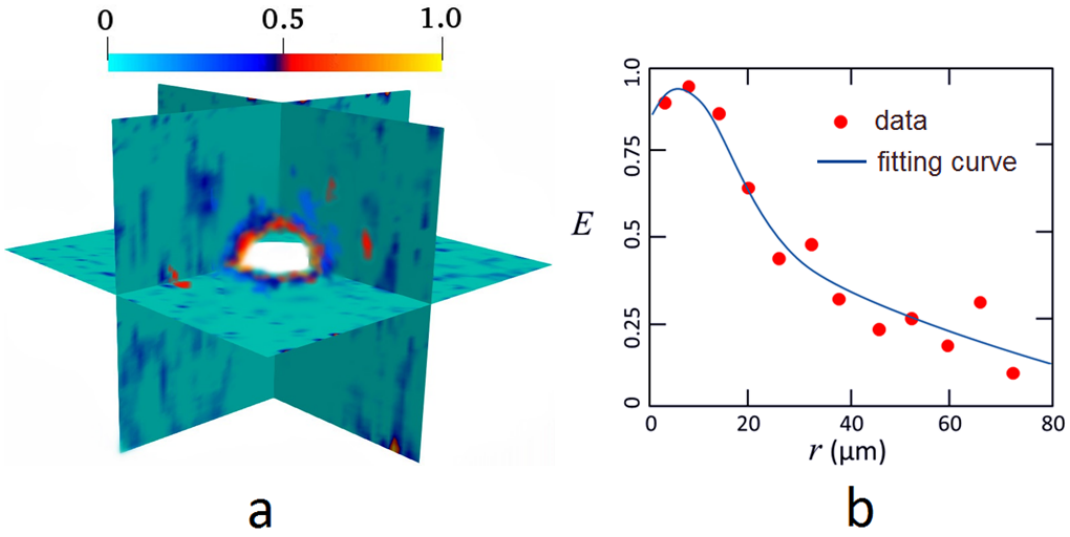


*Figure 2.25 (a) Reconstructed distribution of the normalized modulus within the ECM. The central empty region is occupied by the cell (not shown). The modulus in the vicinity of the cell is significantly larger, which is possible due to the remodeling of the ECM by the cell. The system size is 355 μm (b) Angularly averaged normalized modulus E as a function of the distance r away from the cell surface. Consistent with the 3D visualization, a clear stiffness gradient near the cell surface can be observed.*

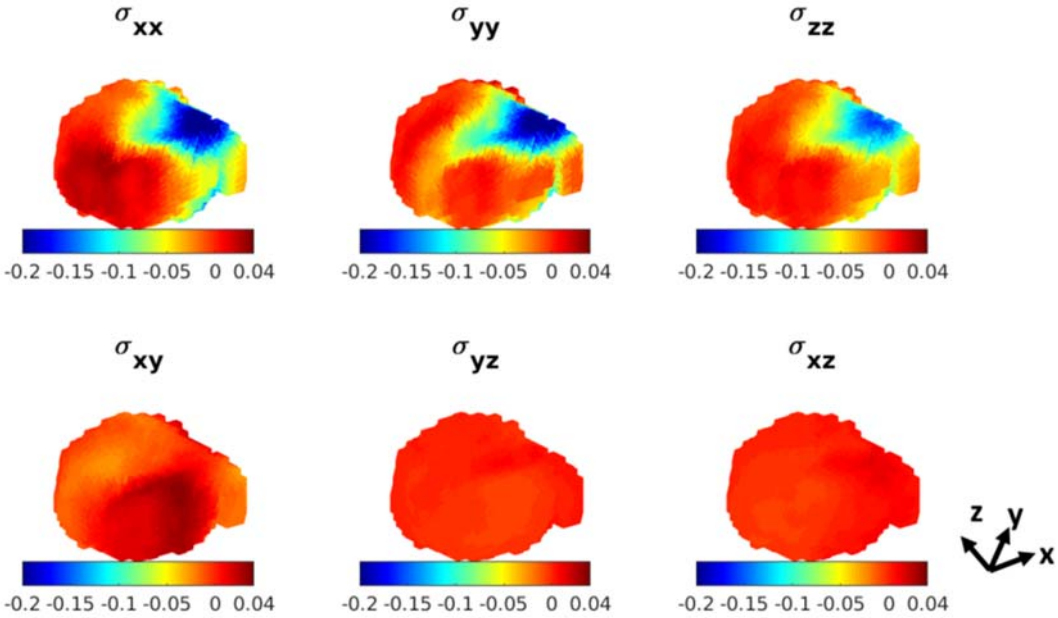


*Figure 2.26 Distribution of normalized stress on cell surface. In the cases of normal stress (i.e., the upper panels), the red region corresponds to cell contraction and the blue region corresponds to a compressive state possibly associated with the development of a local protrusion. The stresses are normalized concerning the overall stiffness of the ECM. The shear stresses are much lower than the normal stresses indicating the cell does not have significant locomotion at the time of observation. These conclusions are consistent with the subsequent dynamics of the cell tracked using confocal microscopy (see Fig. 2.28).*

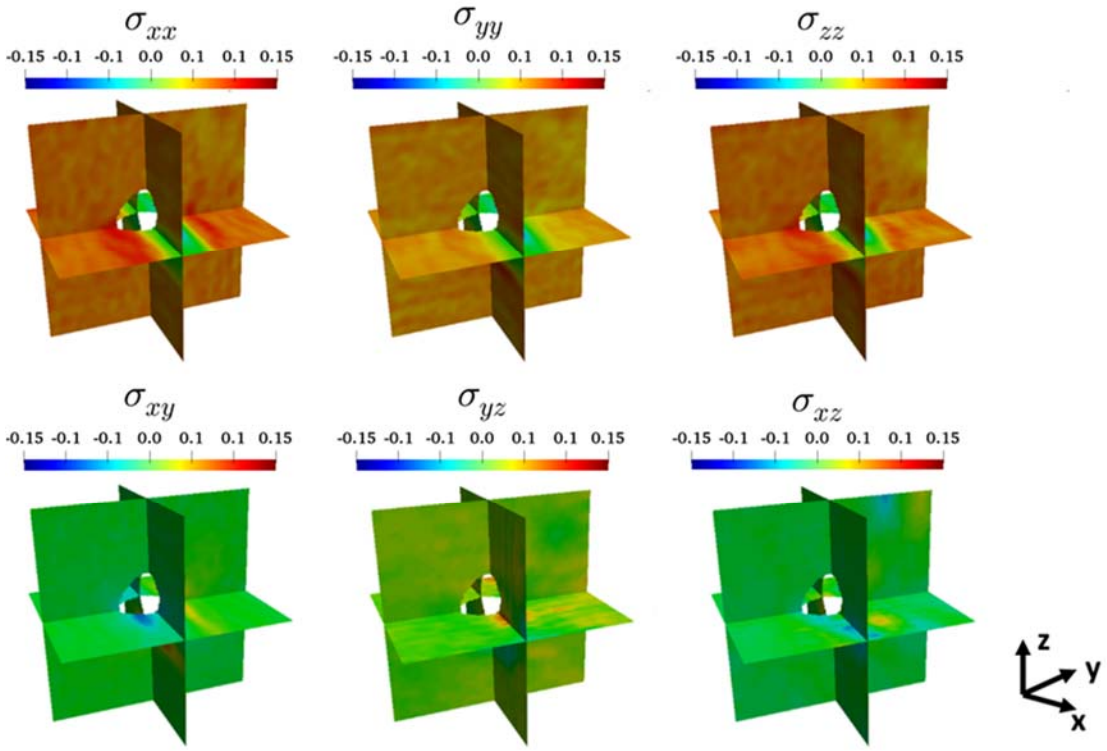


*Figure 2.27 Distribution of normalized stress within in the ECM. $\sigma_{xx}$, $\sigma_{yy}$ and $\sigma_{zz}$ are normal stresses along the three principal directions; positive values indicate pulling state and negative values indicate compression state. A narrow compressive zone can be clearly seen, which is resulted from localized compressive state of cell, associated with the development of local protrusion in that region. $\sigma_{xy}$, $\sigma_{yz}$ and $\sigma_{xz}$ are shear stresses. The stresses are normalized with respect to the average stiffness of the ECM. The shear stresses are much lower than the normal stresses, indicating that the cell does not have significant locomotion at the time of observation.*

Fig. 2.25(a) shows the reconstructed distribution of Young's modulus of the ECM, from which the heterogeneous nature of the modulus distribution can be seen. We note that the far away from the cell, locally stiff regions of ECM generally possess a uniform distribution, which is mainly due to the disordered nature of the collagen network. In addition, the region in the vicinity of the cell surface clearly possesses a higher stiffness, which might be due the ECM remodeling in regions close to the cell. Although the normalized modulus values are used for visualization, the actual modulus values can be easily obtained by a rescaling with respect to the overall average modulus of the ECM, i.e., $\mathrm{E}_0 = 2\ \mathrm{KP}$.

Fig. 2.25(b) shows the angularly averaged local Young's modulus in the 3D reconstruction domain as one moves away from the cell surface. In particular, concentric spherical shells with the thickness dR ≈ 5μm are constructed, with the minimal shell being the circumsphere of the cell. The normalized E values within each spherical shell are averaged and the red circles in the plot show these averaged values. Consistent with the 3D visualization, a clear stiffness gradient can be observed, i.e., as one moves away from the cell surface, the normalized modulus first rapidly decreases and then reaches a plateau value.

Once the distribution of ECM modulus is known, it is straightforward to calculate the stress distribution both on the cell surface and in the ECM region, which is respectively shown in Fig. 2.26 and Fig. 2.27. As can be seen from Fig. 2.26, the cell surface stress distribution indicate that the cell is in a hybrid traction state, with the majority part of the cell generating pulling forces (e.g., the red regions on the cell surface) and a localized region generating compressive forces (e.g., the

blue region on the cell surface). This analysis suggests that the cell is overall actively contracting while a local protrusion is possibly being developed in the compressive region. This is consistent with the emergence of a narrow compressive region in the ECM near the compressive region on the cell surface (see Fig.2.27). The shear stresses (both on the cell surface and in the ECM) are much lower than the corresponding normal stresses, indicating the cell does not have significant locomotion at the time of observation.

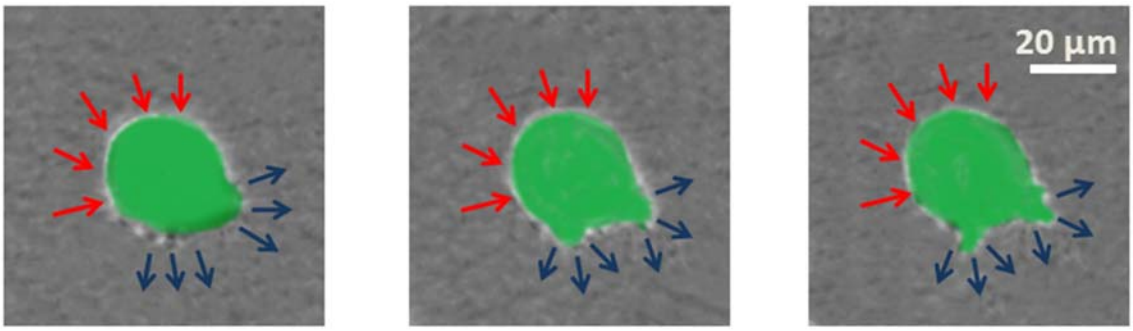


*Figure 2.28 Segmented time-elapse confocal images showing the development of local protrusion on the cell surface at 20 min, 50 min, and 80 min. This is consistent with our traction force analysis, i.e., the regions for local protrusions are in the compressive state (blue arrows) while the majority of the cell surface is in pulling state (red arrows).*

To further verify the traction state obtained above, we track the dynamics of the cell for 2 hours immediately after the acquisition of the displacement data for our analysis using time-elapse confocal microscopy. Figure 2.28 shows the segmented confocal images highlighting the morphology of the cell. It can seem that a local protrusion emerges in the region in the compressive state, which rapidly grows into filopodia. This is consistent with our traction analysis.

# CHAPTER 3

# ACTIVE-PARTICLE-ON-NETWORK MODEL FOR COLLECTIVE CELL MIGRATION

## 3.1 Collective cell migration in three-dimensional ECM

Cell migration in the three-dimensional extracellular matrix (ECM) is a complex dynamic process involving a series of intracellular and extracellular activities [2,74]. Besides the well-established chemotaxis [75], the microstructure and physical properties of the ECM can also significantly influence single cell migration via durotaxis [34,80], haptotaxis [81], and contact guidance [11,12,82]. For example, in durotaxis, a cell can sense and respond to the rigidity gradient in the local microenvironment, which in turn guides its migration [10]. A migrating cell also generates active pulling forces [83], which are transmitted to the ECM fibers via focal adhesion complexes [23,25,84]. Such active forces consistently remodel the local ECM (e.g., by re-orienting the collagen fibers, forming fiber bundles and increasing the local stiffness of ECM) [14,17,44,77–79,112]. Recent studies have indicated that a delicate balance among the magnitude of the pulling forces, the cell ECM adhesion strength, and ECM rigidity is required to achieve an optimal mode of single cell migration [27]. In a multi-cell system, the pulling forces generated by individual cells can give rise to a dynamically evolving force network (carried by the ECM fibers) in the system [15,22]. The force network can further influence the migration of the individual cells, which in turn alters the ECM and the force network. This feedback loop between the force network and cell migration could lead to a rich spectrum of collective migratory behaviors. Although guided cell migration via ECM-mediated mechanical cues has recently been investigated [113], the evolution of the force network in ECM due to multi-cell migration, its role in regulating collective migratory behaviors, and in the emergence of possible self-organizing multicellular patterns remain to be elucidated.

### 3.2 Generation and structural properties of the random network model

First, a random network model is generated to accommodate collective cell migration analysis. The random network models used in the simulations are generated based on the maximally random jammed (MRJ) packing configurations, which are obtained using the Lubachevsky-Stillinger algorithm [114]. In particular, starting from a low-density configuration of small non-overlapping spheres randomly distributed in the simulation box, each sphere is given a random velocity. The particles follow Newton's law of motion, colliding with each other as they move and each particle also grows (i.e., isotopically expand) with a prescribed growth rate. The simulated is terminated once a jammed packing of the spheres, characterized by a diverging collision rate, is obtained (see *Figure 3.1*).

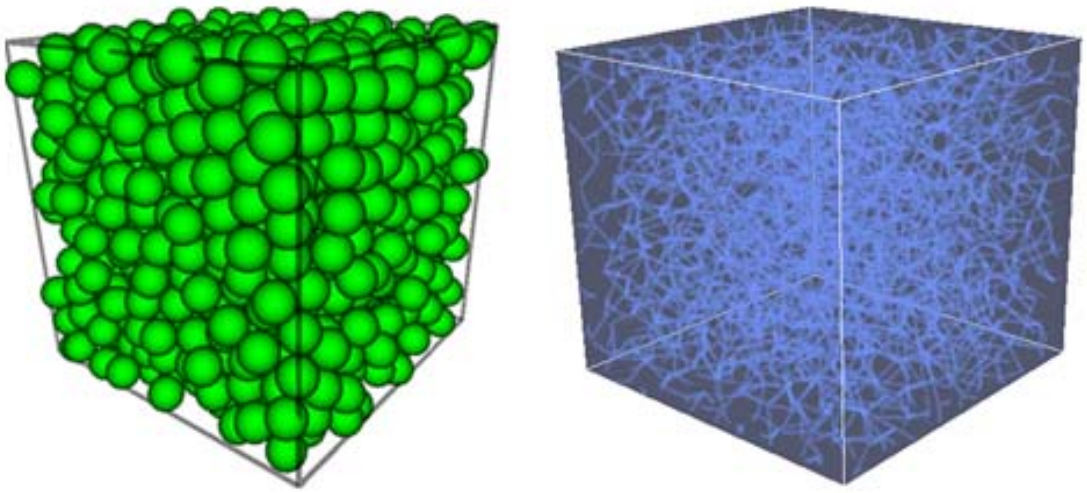

*Figure 3.1 Left panel: A typical maximally randomly jammed packing configuration of equal-sized spheres generated using the Lubachevsky-Stillinger algorithm. Right panel: A random network model can be derived from this packing by connecting the spheres touching each other.*

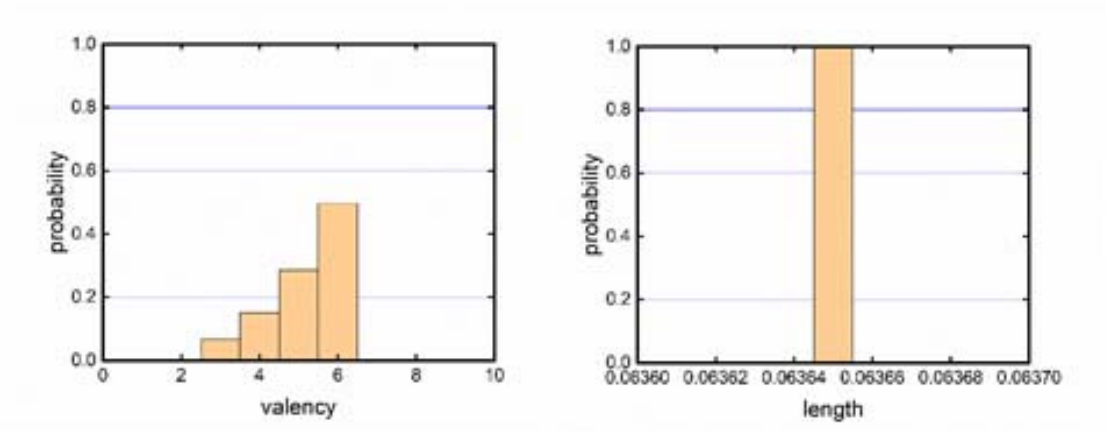


*Figure 3.2 Structural statistics of random networks derived from MRJ packings. Left panel: distribution of coordination number. Right panel: distribution of bond length.*

Once the MRJ packings are obtained, the sphere centers are mapped to the nodes of a network, and each pair of the contacting spheres are connected by a bond. This leads to a random isostatic network with an average coordination number Z ≈ 6. *Figure 3.2* shows the structural statistics of random networks derived from MRJ packings, including the distribution of coordination number, the distribution of bond length. It can be seen that the bond lengths are very uniform and the overall network is statistically isotropic.

### 3.3 APN model, minimal model for tumor cell migration following local durotaxis

Here, we make an attempt to understand the collective cellular dynamics in 3D ECM resulted from the dynamically evolving force network, using a minimal active-particle-on-network (APN) model. In particular, the 3D ECM is modeled as a discrete network with a *graph* (i.e., node-bond) representation in a cubic simulation domain with linear size L, which is composed of $M_n$ nodes and $M_b$ bonds. The average coordination number Z, i.e., the average number of bonds connected to each node, is given by $Z = 2M_b/M_n$. We have used both the periodic boundary (PB) conditions and fixed boundary (FB) conditions (i.e., the nodes within a certain distance δL from the

boundaries of the simulation domain are fixed) in our simulations, and find that even for a moderate system size (e.g., $M_n$ ~ 5000) the boundary conditions do not affect the results. In the subsequent discussions, we will mainly present the results obtained using the fixed boundary conditions, under which $M_n$ denotes the number of free (non-fixed) nodes.

Still, a similar micro-mechanical model of fiber in collagen-based ECM network is applied in APN model. The bonds of the network are modeled as elastic elements with only non-zero stretching modulus $E_s$ and free to rotate at the nodes. An active particle can generate pulling forces in the bonds connected to the node it occupies by contraction, i.e., $\delta l$. This contraction leads to a strain $\varepsilon_i = \delta l/l_i$ in the bond i with original length $l_i$, and thus, a pulling force $f_s = E_s \cdot A \cdot \delta l/l_i$, where A is an effective cross-sectional area of the bonds. These pulling forces impose force boundary conditions for the ECM network, and the force-balance network configuration is obtained using an iterative force-based relaxation approach [21].

Next, $N_p$ active particles (e.g., congruent spheres) which are representing cells are introduced in the network such that each particle occupies a randomly selected un-occupied node (i.e., each node can be occupied by only one particle). The number density $\rho$ of the particles is defined as $\rho = N_p/M_n$, i.e., the fraction of nodes occupied by the active particles. Each particle can generate a contraction, which pulls all of the bonds connected to the node it occupies towards the particle center (i.e., the node) by a fixed amount $\delta l$, leading to different pulling forces in the bonds and thus, a force network in the system. The force network system established by pulling force of the particles is similarly generated compared with the force network we discussed in Part 2.4.

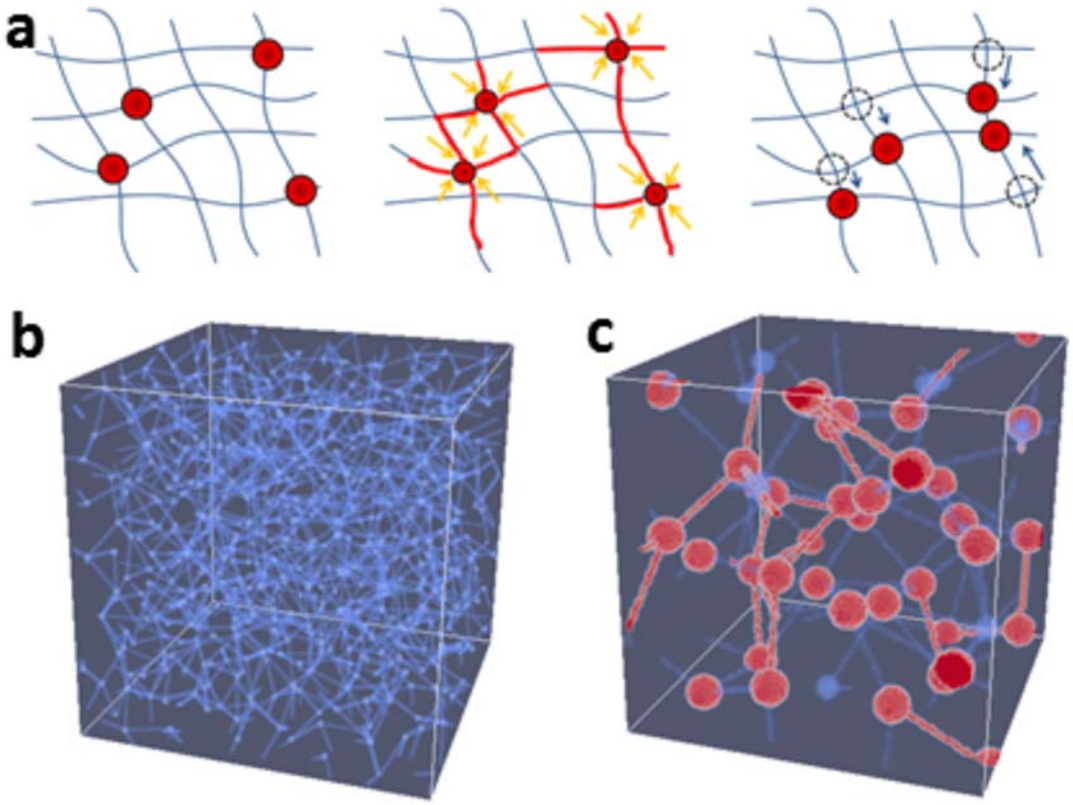


*Figure 3.3 (a) Schematic illustration of the active-particle-on-network (APN) model. Left: Particles on a stress-free network. Middle: Particle contraction leads to a force network composed of high-stress fibers (illustrated using red). Right: Particles migration on the ECM network along fibers carrying the largest forces. (b) A realization of the random network model generated based on maximally random jammed sphere packing. (c) Force network (carried by the high-stress fibers) generated by contractile particles (shown as red spheres) on the network.*

We consider the particles can *migrate* from its original node to an un-occupied neighboring node following local durotaxis, i.e., along with the bond with the highest stiffness, which is also the bond that carries the largest pulling force among all neighboring bonds (see *Figure 3.3* for illustration). The diameter of the particles is not essential in our model and thus, is not explicitly considered here.

We note that even in this minimal model, many factors can affect the interactions between the dynamic force network and the collective dynamics of the active particles. These may include the geometry/topology and mechanical properties of the ECM network, as well as the number density, spatial distribution and the contractibility (i.e., $\delta l$) of the active particles. In this work, we mainly focus on disordered networks derived from maximally random jammed packings of congruent hard spheres [115], which are isostatic (i.e., with $Z = 6$). We note that it is straightforward to generalize this study to random network models derived from confocal images of collagen gels [116]. In addition, we use simple linear elastic models for the bonds and consider that the nodes cannot resist torques. This allows us to investigate the system in the elastic regime [66]. In this case, the force network is mainly determined by the number density and spatial distribution of the active particles, and largely independent of particle contractibility.

Besides, our model can readily incorporate more realistic mechanical models for the ECM, taking into account various nonlinear responses of the fibers including strain hardening [67,97] and plasticity [14]. Moreover, in an actual cell ECM system, the cell migration might not be sensitive to individual stiffer fibers, but determined by certain mesoscale stiff structures emerged due to cell remodeling, such as bundles of high-stress fibers. Nonetheless, we believe that the general organizational principles of active particles on random networks obtained here are relevant to and can provide insights on the actual cell-ECM systems.

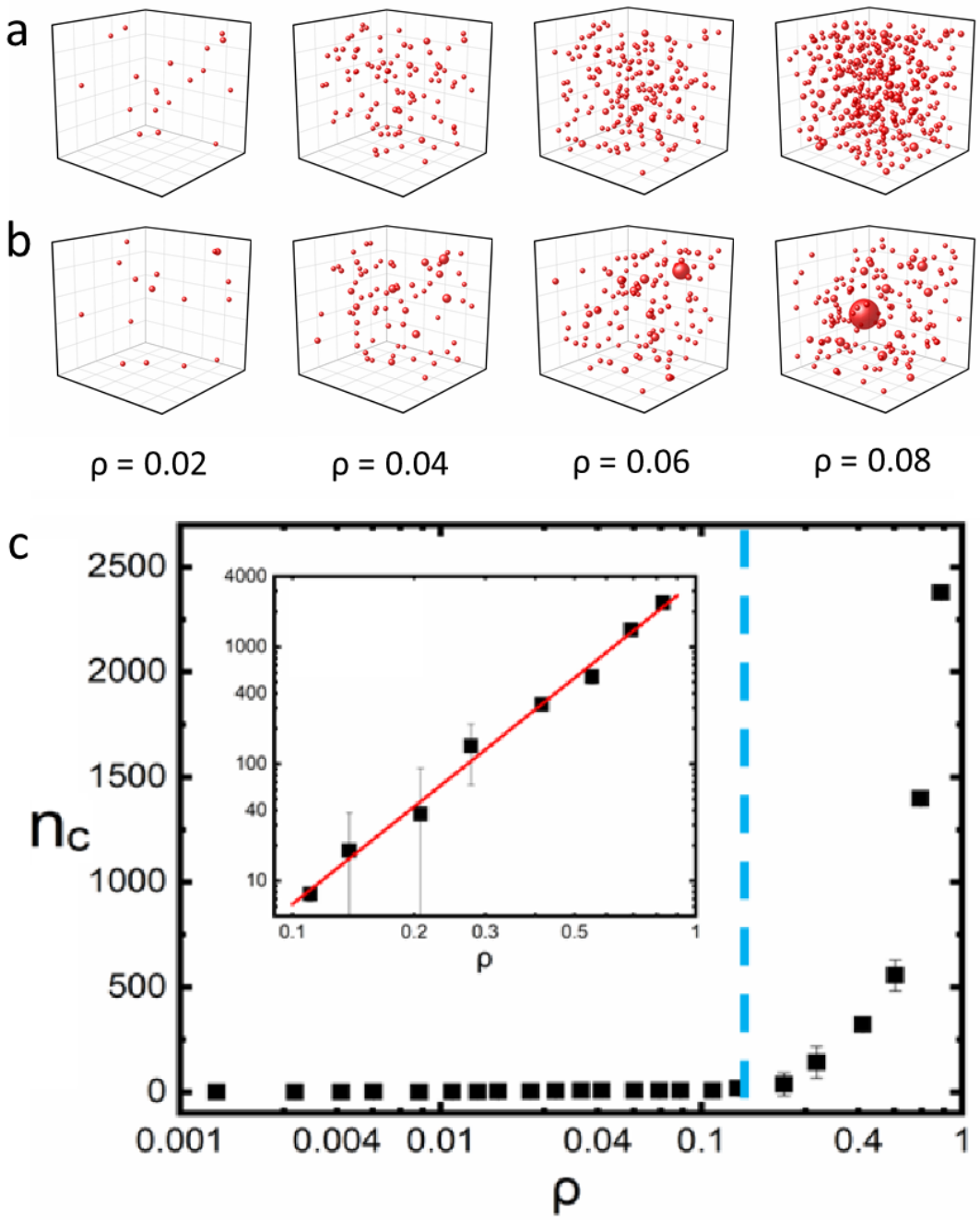
a
b
ρ = 0.02
ρ = 0.04
ρ = 0.06
ρ = 0.08
c
2500
2000
1500
1000
500
0
$n_c$
0.001
0.004
0.01
0.04
0.1
0.4
1
ρ
4000
1000
400
100
40
10
0.1
0.2
0.3
0.5
1
ρ

*Figure 3.4 (a) Initial distribution of clusters formed by randomly placed active particles on the network for different number densities ρ. In these plots, a cluster is represented by a sphere for better visualization with the center coinciding with the center of the cluster and the radius representing the cluster size. (b) Distribution of clusters in the final state of the APN system. As ρ increases, the particles tend to aggregate into a single large cluster in the system. (c) The normalized maximal cluster size nc as a function of ρ. A transition behavior is apparent as ρ approaches ρc ≈ 0:0694 from below. The statistics are obtained by averaging over 20 independent simulations.*

### 3.4 Dynamic phase transition in the APN system

We now describe the observed collective dynamics of the active particles on random networks. In our simulations, we systematically vary the particle number density ρ between 0:05 and 0:95. For each ρ, the particles are initially randomly introduced in the network and the system is allowed to evolve according to the aforementioned APN dynamics. At low densities (i.e., $\rho < \rho_c \approx 0:0694$), the particles rapidly aggregates into multiple isolated small clusters, which are randomly distributed within the ECM, as shown in *Figure 3.4(a)* and *Figure 3.4(b)*.

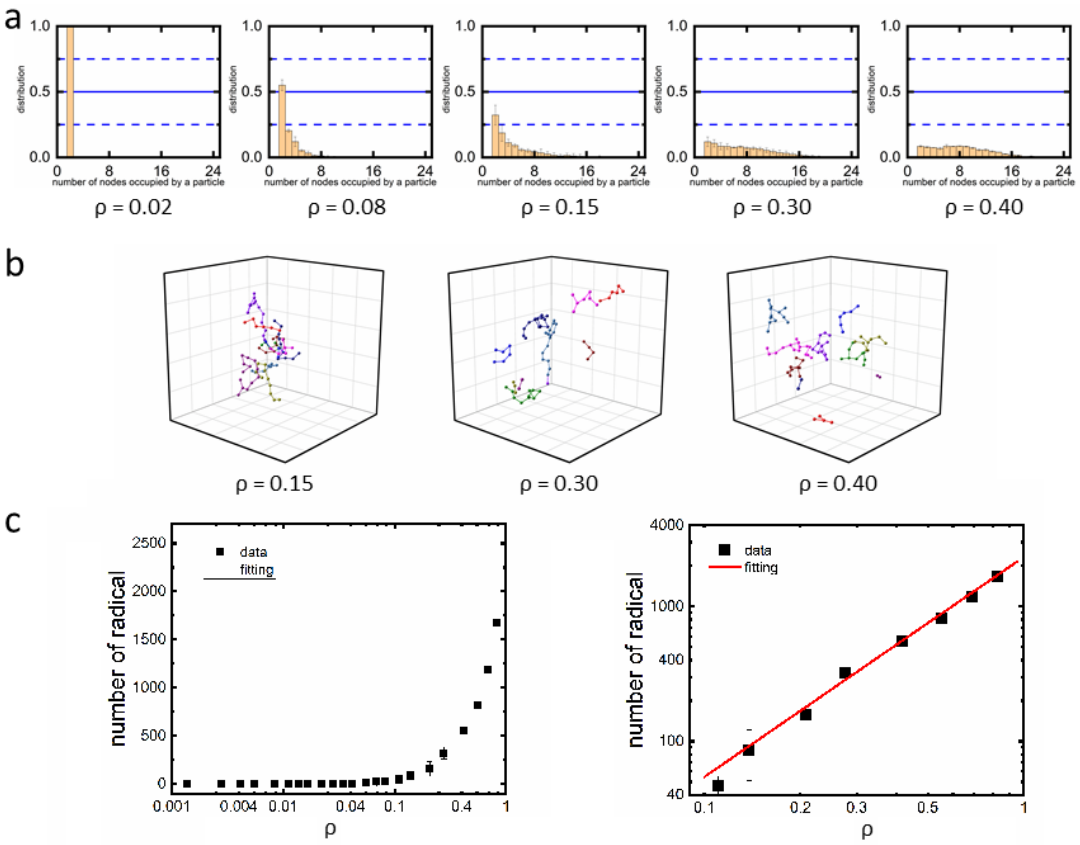


*Figure 3.5 (a) Statistics of the number of distinct nodes ms visited by a particle for s = 20 successive steps for different number densities ρ. (b) Representative trajectories for randomly selected radicals (i.e., highly dynamic particles) for different ρ. (c) The number of radicals Nr as a function of ρ, which exhibits a clear transition at ρc = 0:0694. This is consistent with the transition observed in the maximal cluster size nc as ρ increases (See Figure 3.4(c)).*

Here, we consider two particles belong to the same *cluster* if their occupied nodes connected by a bond. A cluster of the active particles on the network is a set of particles for which there is a connected path between any two particles. The normalized maximal cluster size $n_c$ is defined as $n_c = N_{max\text{-}c}/N_p$, where $N_{max\text{-}c}$ is the number of particles in the largest cluster of the system

and $N_p$ is the total number of particles. In the case of dynamic clusters, the cluster size is the average over s = 500 evolution steps.

As ρ approaches $\rho_c$ from below, the normalized maximal cluster size $n_c$ increases dramatically, shown in *Figure 3.4(c)*, indicating the majority of the particles are connected to form a single large cluster in the system. In addition, we find that the isolated small clusters associated with $\rho < \rho_c$ are stationary, i.e., the particles in the clusters either do not move at all or hop between two adjacent nodes (typically at the boundary of a cluster). On the other hand, the dominant large clusters formed for $\rho > \rho_c$ undergo constant dynamic reorganization. To further quantify the dynamics of the clusters, we count the number of distinct nodes $m_s$ visited by a particle during a total of s successive steps. The collected statistics for different ρ values are shown in *Figure 3.5(a)*. We note that the $m_s$ statistics are shown in *Figure 3.5(a)* does not depend on s and we have used s = 20 here. It can be seen from *Figure 3.5(a)* that for small ρ, a particle can only visit one or two nodes, respectively indicating that the particle does not move or can hop between two adjacent nodes. As ρ increases, although the majority of particles are localized (indicated by the peak in the $m_s$ statistics associated with small node numbers), a small subset of highly dynamic particles emerge which are able to visit many distinct nodes for a given number of steps (indicated by the emergence of the second peak associated with large node numbers in the $m_s$ statistics). We refer to these highly dynamic particles as *radicals* and the trajectory of a small number of randomly selected radicals are shown in *Figure 3.5(c)* for different ρ values. *Figure 3.5(c)* shows the number of radicals $N_r$ as a function of ρ. It can be seen that $N_r$ exhibits a clear transition as ρ increases towards $\rho_c$. This is consistent with the transition observed in the maximal cluster size $n_c$ as ρ increases (see *Figure 3.4(c)*). The above analysis suggests that the system possesses a phase-transition-like behavior, as the particle number density ρ increases, from an *absorbing state* in which the particles segregate into small isolated stationary clusters, to a *dynamic state*, in which the majority of particles join in a single large dynamic cluster. This transition is also quantitatively manifested in the maximal cluster size $n_c(\rho)$ (shown in *Figure 3.4(c)*) and radial number $N_r(\rho)$ (shown in *Figure 3.5(c)*) as ρ increases towards $\rho_c$. In particular, our scaling analysis shows that as $\rho_c$ is approached from above,

$$\boldsymbol{n_c} \sim (\rho - \rho_c)^{\alpha}$$

Where the critical exponent $\alpha \approx 6.7$. In addition, we find that

$$\boldsymbol{N_r} \sim (\rho - \rho_c)^{\beta}$$

Where the critical exponent $\beta \approx 1.75$

### 3.5 Influence sphere due to active pulling forces

We now investigate the mechanisms for the observed transition in the APN system as ρ increases. We first note that it is not surprising that the particles tend to form large aggregates in the ECM network as the number density increases. This is because when a particle pulls the fibers connected to the node it occupies, a stress gradient is built up, with decreasing pulling forces on the fibers as one moves away from the contracting particle. When another particle *senses* the pulling force [28], it will tend to move up the stress gradient towards the contracting particle due to local durotaxis [10,80,113]. This would lead to effective mutual pulling between the particles.

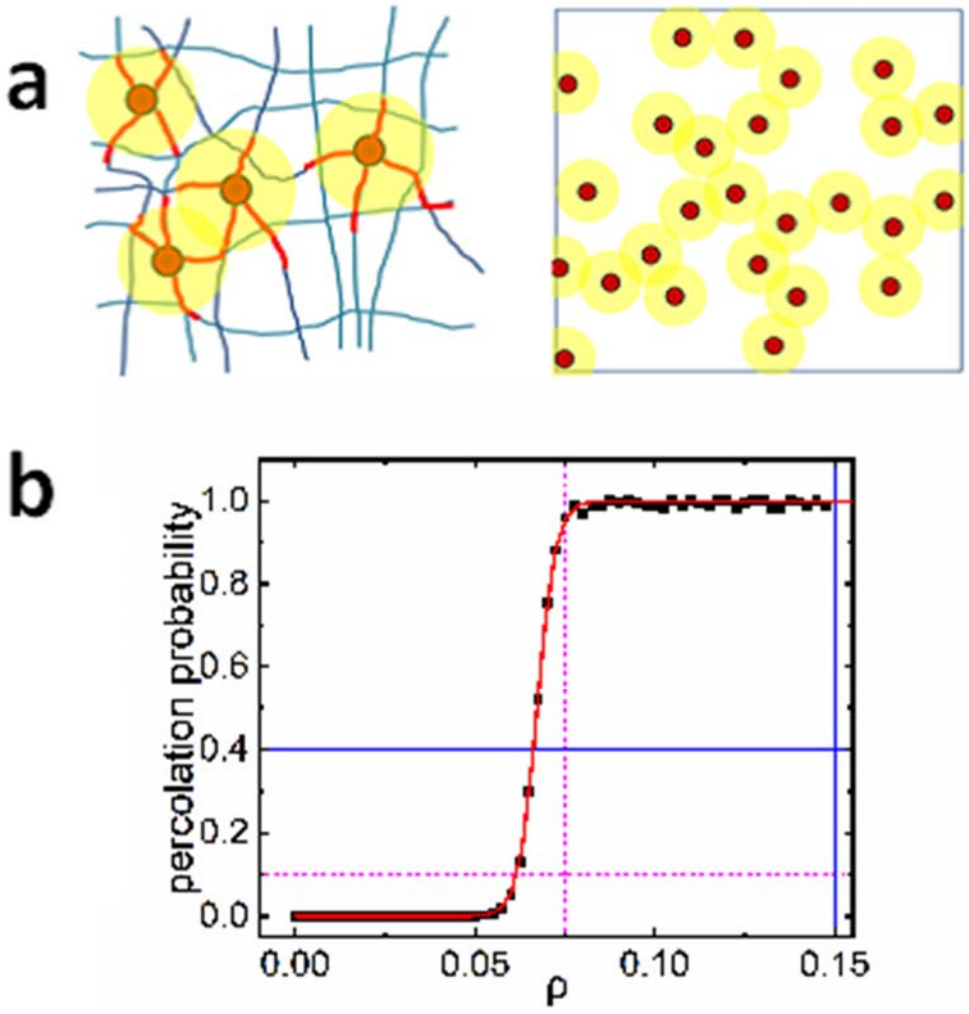


*Figure 3.6 (a) Schematic illustration of the concept of the influence region (yellow circles), characterizing the range of the pulling forces (red) due to particle (red) contraction. (b) Percolation probability analysis indicates a percolation transition of overlapping influence spheres with radius RI = 0:052L at ρ* = 0:0672, which coincides with the critical density ρc = 0:0694 for the dynamic phase transition in the APN system.*

Moreover, it is reasonable to assume that the pulling forces generated by a specific particle can only influence the particles within a certain distance $R_I$ from the contracting particle, which mainly depends on the properties of the ECM network. In general, due to the intrinsic heterogeneity of the ECM network, the value of $R_I$ may vary for different particles and the same particle at different nodes (locations). Here, we take a *mean-field* approach and assign the same effective $R_I$ to all the particles in the system during the entire evolution of the system. This allows us to introduce the concept of the influence sphere, which is a spherical region with radius $R_I$ centered at a contractile particle (see *Figure 3.6(a)*). The radius of the influence sphere $R_I$ can be estimated from the cluster statistics of the APN systems with low ρ, i.e., those containing multiple small isolated stationary clusters in the final state. This is based on the assumption at low ρ, only particles which are within the influence region of one another would eventually aggregate. In particular, we first identify the particles within the same (well-defined) cluster in the final state of the system. Then the system is *re-winded* to the initial state (i.e., when the particles are placed on randomly selected nodes of the ECM network), and the intra-cluster nearest-neighbor distances $d_n$ (i.e., the shortest distance between a specific particle and any other particles in the same cluster) are computed for all clusters. We then use the mean nearest-neighbor distance $\overline{d_n}$ to estimate $R_I \approx 0{:}052L$ (where L is the edge length of the simulation domain).

### 3.6 Mean field theory: Percolation of influence sphere

We now investigate the percolation of the influence spheres as the number density ρ increases. In particular, for a given density ρ, we randomly introduce the particles in the ECM network, identical to the procedure for generating initial configurations for the aggregation simulations. However, instead of allowing the particles to move according to the dynamical rules, we now place a virtual sphere with radius $R_I = 0{:}052L$ at each particle, representing the influence sphere for this particle. We subsequently identify the clusters formed by the influence spheres (i.e., two overlapping spheres are considered to belong to the same cluster), and determine the maximal cluster size $l_c$ (i.e., the linear dimension of the largest cluster formed by the overlapping virtual

influence spheres along the three orthogonal directions, in the unit of the edge length of the simulation box), based on which the percolation of the system can be determined. *Figure 3.6(b)* shows the percolation probability for the system [117], from which a percolation transition and the associated critical number density (i.e., percolation threshold) $\rho^* \approx 0{:}0672$ can be clearly identified.

The percolation threshold associated with the influence sphere is determined using a percolation probability analysis. In particular, for a given particle number density $\rho = N_p/M_n$ (where $N_p$ is the number of particles and $M_n$ is the total number of available nodes in the network), a total of $X_C = 100$ independent configurations are generated. Each configuration is generated by randomly selecting Np nodes from the given network and placing an influence sphere with radius $R_{in}$ centered at the selected node. Next, we identify the largest cluster formed by the overlapping influence spheres and check whether this cluster spans the entire system. If a system spanning cluster is identified, the system is considered percolated. The total number of percolated systems for a given particle number density is then obtained, i.e., $X_p(\rho)$, and the percolation probability for the system at number density ρ is computed as: $P(\rho) = X_p(\rho)/X_C$. Following this procedure, the percolation probability P(ρ) for all ρ of interest can be computed (as shown in *Figure 3.6* of the main paper).

To estimate the percolation threshold ρ* for the system, we approximate the percolation probability P(ρ) with the following function [118]:

$$P(\rho) = \frac{1}{2}\left[1 + \tanh\left(\frac{\rho - \rho^*}{\Delta}\right)\right]$$

Where $\Delta$ is the effective *transition width*, which decreases with system size. By fitting the numerical data for P(ρ) using the above equation, we can obtain ρ*accordingly, i.e., ρ*=0.0672.

Interestingly, the percolation transition of the influence spheres coincides with the dynamic transition of the active particles at the same $\rho_c \approx 0{:}0694$. This suggests that the dynamic transition of the active particles from the *absorbing* state to the *dynamic* state is underlaid by and can be understood as the percolation transition of the influence spheres.

Finally, we emphasize again that this minimal model does not take into account crucial mechanisms in actual cell migration such as ECM remodeling (e.g., orientation, bundling and

degradation) and cell-cell adhesion. Interestingly, our studies indicate that, at least for the APN systems, the local durotaxis for the active particles is sufficient to induce and stabilize aggregations, even without adhesion. Nonetheless, we expect that the insights on the collective behaviors of active particles regulated by the dynamically evolving force network obtained here are helpful in understanding the collective dynamics emerged in actual multi-cellular-ECM systems.

### 3.7 APN model explaining mechanical-induced tumor cell invasion

In this part, a novel experiment is designed to help to understand the collective multi-cellular dynamics induced by the ECM-mediated mechanical coupling of the cells. Normally, the coupling is very difficult to observe directly. Using our APN-model, a collective *pulling effect* of the aggregation behavior is well established showing that in the lateral direction, induced by the ECM-mediated transmission, active contractile forces are generated by the polarized migrating cells.

Here, we explicitly consider the mechanical coupling between distant cells through ECM network mediated stress propagation [19,21,22,27,113]. Previously developed active-particle models for multicellular systems typically impose an ad hoc interaction (e.g., alignment interaction) among nearby cells, without explicitly considering the underlying mechanisms [119,120]. Here, we consider the cell motion follows the over-damped Langevin equation

$$\frac{d\mathbf{r}_i(t)}{dt} = \mu_i \left[ \sum_j \mathbf{F}_{ji}(t) + \mathbf{F}_{ECM}(t) + f_i \mathbf{e}_i(t) \right] + \eta_i \mathbf{u}_{rand}(t)$$

Where ri is the position vector of cell i; fi is associated with the persistent velocity (i.e., cell mobility) depending on the micro-environment (e.g. 2D substrate vs. 3D Matrigel) and its direction is specified by the unit vector $\mathbf{e}_i$, which is subject to rotational diffusion; $\mathbf{u}_{rand}$ is a random unit vector, $\mathbf{F}_{ji}$ is the intercellular force between cell i and j upon contact, $\mathbf{F}_{ECM}$ is the total force that ECM exerts on the cell and is only non-zero for cells in the ECM region, $\mu_i$ and $\eta_i$ respectively characterize the cell's response to external forces and random drift. Cell mobility for different types of cells in different micro-environments is calibrated based on experimentally obtained individual cell

dynamics. The intercellular contact force **F**ji is repulsive when the two cells (modeled as deformable spheres) are too close to one another (due to cytoplasm exclusion volume), and decays to zero as the cell center distance increases and then becomes adhesive for a finite range [120].

The Matrigel is modeled as a nonlinear 3D network with a bond-node representation [17,18,97]. The cells in the ECM network, modeled as deformable spheres, can generate active forces by pulling the nodes close to the cell surface (mimicking focal adhesion sites) via isotropic contraction [21], and sense the total force $\mathbf{F}_{ECM}$ exerted on the cell via the bonds attached to it. Thus, the active force generated by a contractile cell can propagate via the ECM network to a distant cell and subsequently influence its migration and vice versa. When multiple cells are present in the 3D ECM network, our model simulates collective migration dynamics that are partially regulated by the dynamic force network generated by the actively migrating cells.

Consistent with experimental results, stronger dynamic correlations are observed for the cells in 3D Matrigel compared to those in the 2D substrate (with a correlation length a ≈ 12 μm). Importantly, for the simulated cell systems with random cell velocities, the dynamic correlation among the cells (with a ≈ 20 μm) is much weaker than that in systems with collective polarization (a ≈ 27 μm). We note that for collectively polarized cells, we only computed velocity correlations in the non-polarized directions. This suggests that collective polarization is necessary for our system to induce sufficient ECM-mediated mechanical coupling leading to the overall aggregation behavior.

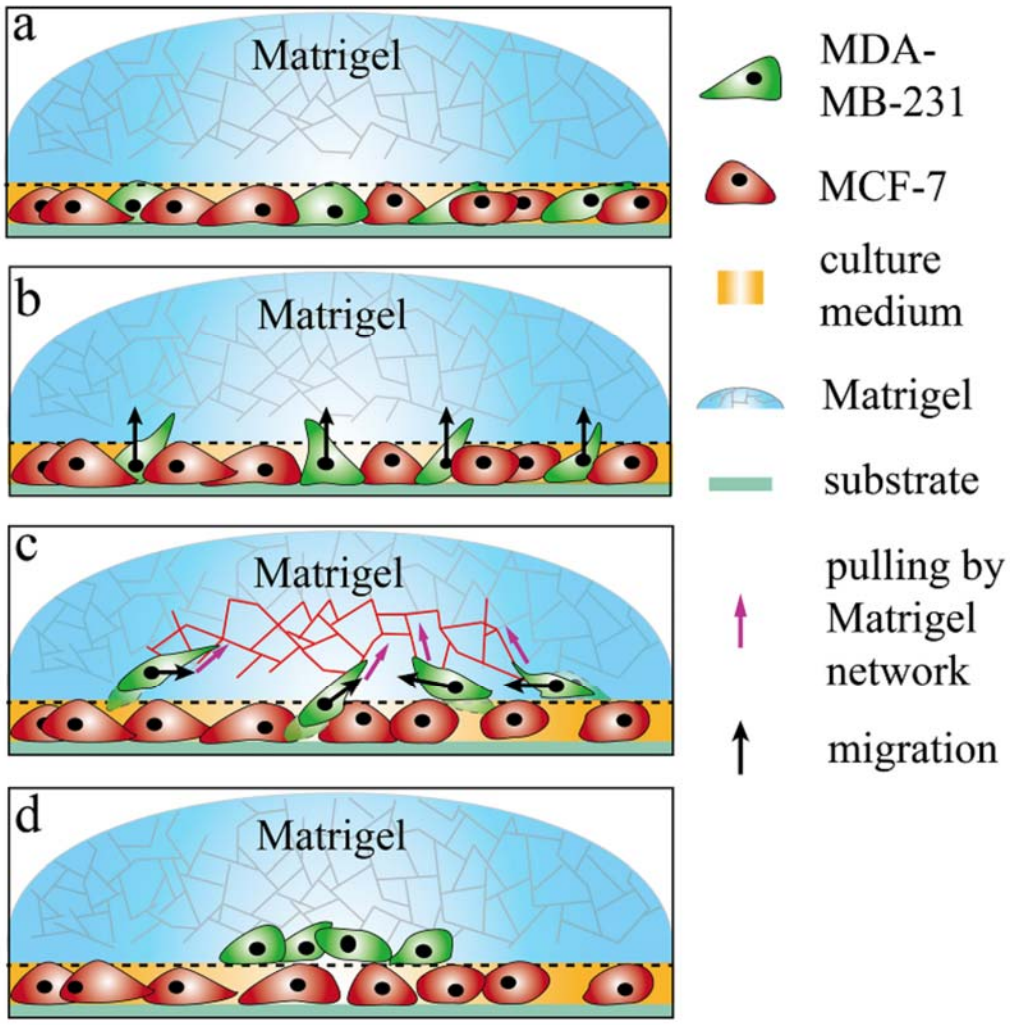


*Figure 3.7 Schematic illustration of the abnormal aggregation of invasive MDA-MB-231 cells induced by collective polarization and ECM-mediated mechanical coupling. (a) MDA-MB-231 cells are co-cultured with MCF-7 cells covered by a Matrigel layer. (b) MDA-MB-231 cells massively invade into the upper Matrigel region, leading to strong collective polarization. (c) Polarized migrating cells generate effective pulling forces due to cell contraction via the ECM network. (d) Aggregation results from the ECM-mediated mechanical coupling among the polarized cells.*

In summary, our comprehensive experimental and computational investigations indicated that the abnormal aggregation behavior of invasive tumor cells results from the strong collective polarization of cell migration and the resulting ECM-mediated mechanical coupling. This mechanism is schematically illustrated in *Figure 3.6*. To the best of our knowledge, this is the first report of direct observation of collective multi-cellular dynamics induced via ECM-mediated mechanical coupling of the cells. Our results also indicate the importance of explicitly incorporating the micro-environment into active-particle theories for multi-cellular systems, specifically in explaining the collective behaviors of cancer cells during the invasion process. We note that it is not uncommon for invasive tumor cells to exhibit local collective polarization. Therefore, the ECM-induced mechanical coupling of collectively migrating cells could be a potential factor driving metastatic cell aggregation in the clinical invasion.

# CHAPTER 4

# FUTURE WORKS

## 4.1 Future work for reconstruction and micro-mechanical analysis in ECM

In future work, more circumstances of cell migration in heterogeneous ECM network will be built up to mimic more situations for cell migrations for both malignant cells and non-malignant cells, such as peripheral neuroblastic tumors metastasis [121], leukocyte transendothelial migration [122], lymphocyte migrations [123], tendon healing [124] and etc.. The interpretation and mechanisms of the migration will be further explains using the model established. In the meantime, the reconstruction method and the mechanical model should be specifically modified to fit different usages. Besides, in order to mimic the real in vitro or in vivo situation, modifications of the model will be employed such as adding heterogeneity of fiber orientation in the random local area, adding cell with multiple/variable of contracting focal points *etc.*.

In the current model, a free ECM network is presented for cell migration, the source of the pulling force comes from the contraction of the cell, as shown in *Figure 4.1(A)*. But in most circumstance, an external force might domain the micro-mechanical environment in the migrating area. In that case, a pre-stressed network can be established to interpret migration behavior. Thus, the mechanism of migration behavior will be compared.

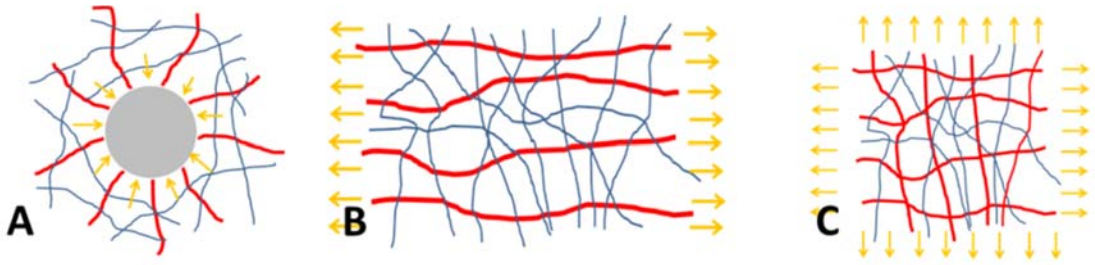


*Figure 4.1 Schematic illustration of three representative macroscopic loading conditions for inducing mechanical cues in APN systems: (A) concentric contraction, (B) uniaxial tension, and (C) tri-axial tension. The force chains composed of high-stress fibers are highlighted using red color.*

Also, the cell model used for generating the mechanical forces can be also replaced with an advanced model in which the cell morphology can mimic the real cell scanned by confocal microscope from experiments. Although the ellipsoid cell model is simplified from the real breast tumor cell, it still needs to be modified to fit other migrating cells. Specifically, we can substitute the cell model by subcellular element model. This model will further improve the reality of the cell contraction and the force propagate from the cell. And eventually, further recover the interaction between cell and ECM.

Still, we are aiming to build up a model that can interpret how the mechanic force would influence the collective immigrating behavior of the tumor cell. A system will be established with a force field generated by the motion of a migrating cell and preserved by the ECM network. But more foundational studies elaborated above are needed before the collective migration behavior could be explained by the force-field model.

### 4.2 Future work for APN model for collective cell migration

We will further investigate the detailed dynamics of the individual active particles in the large dynamic cluster associated with high particle number densities, in order to better understand the observed statistics. We will investigate whether there would be any stable local dynamic patterns associated with the hopping particles. In addition, we will carry out a detailed analysis of the formation of the clusters, as a possible critical phenomenon. In particular, we will investigate the average cluster size NC (number of particles included in a cluster) as a function of particle number density ρ. We expect to observe a transition of the behavior this quantity NC at a critical ρc (i.e., from very slow growth to a sudden rapid growth as ρ increase). If identified as a critical phenomenon, the universality class which this transition belongs to will be determined.

Still, as we discussed in Part 4.1, we would also investigate how the pre-stressed network bias will cue the collective behavior of the moving active particles. An important question that we will address in all the cases is: what magnitude of the external cues (e.g., compared to the particle contractility) would be sufficient to significantly influence collective cell migration? For example, besides the expected behaviors we discussed above which are mainly determined by the pre-stressed network, we also expect to observe a regime that externally applied cues and particle contractility play similar roles, and will systematically investigate the self-organization behaviors in this regime.

We will further refine and generalize the percolation-based mean-field theory. For example, for an anisotropic network (e.g., one with fibers aligned in a preferred direction), the force-influence cannot be a spherical shape as in the isotropic network case. It is more likely to be an ellipsoid, which we will verify numerically. In addition, we expect the aspect ratio of the ellipsoid to increase with increasing degree of fiber alignment. In this case, percolation theories for non-spherical particles will be employed.

We expect that the cell-cell adhesion would further stabilize the cell clusters, and thus enhance aggregation in the system. The ECM degradation would suppress force transmission (by destroying the local structural integrity of the ECM network), and ECM remodeling (forming aligned

fibers) would enhance force propagation. These will be verified and investigate quantitatively via extensive simulations with more parameter involved.

REFERENCES


[1] H. Lodish, A. Berk, S. L. Zipursky, P. Matsudaira, D. Baltimore, and J. Darnell, *Molecular Cell Biology. 4th Edition* (2000).

[2] A. J. Ridley, M. A. Schwartz, K. Burridge, R. A. Firtel, M. H. Ginsberg, G. Borisy, J. T. Parsons, and A. R. Horwitz, Science (80-. ). **302**, 1704 (2003).

[3] J. D. Humphrey, E. R. Dufresne, and M. A. Schwartz, Nat. Rev. Mol. Cell Biol. **15**, 802 (2014).

[4] C. Bonnans, J. Chou, and Z. Werb, Nat. Rev. Mol. Cell Biol. **15**, 786 (2014).

[5] R. J. Pelham and Y. -l. Wang, Proc. Natl. Acad. Sci. **94**, 13661 (1997).

[6] T. Yeung, P. C. Georges, L. A. Flanagan, B. Marg, M. Ortiz, M. Funaki, N. Zahir, W. Ming, V. Weaver, and P. A. Janmey, Cell Motil. Cytoskeleton **60**, 24 (2005).

[7] A. J. Engler, S. Sen, H. L. Sweeney, and D. E. Discher, Cell **126**, 677 (2006).

[8] K. R. Levental, H. Yu, L. Kass, J. N. Lakins, M. Egeblad, J. T. Erler, S. F. T. Fong, K. Csiszar, A. Giaccia, W. Weninger, M. Yamauchi, D. L. Gasser, and V. M. Weaver, Cell **139**, 891 (2009).

[9] R. W. Tilghman, C. R. Cowan, J. D. Mih, Y. Koryakina, D. Gioeli, J. K. Slack-Davis, B. R. Blackman, D. J. Tschumperlin, and J. T. Parsons, PLoS One **5**, (2010).

[10] E. Hadjipanayi, V. Mudera, and R. A. Brown, Cell Motil. Cytoskeleton **66**, 121 (2009).

[11] S. Guido and R. T. Tranquillo, J. Cell Sci. **105 ( Pt 2**, 317 (1993).

[12] P. P. Provenzano, D. R. Inman, K. W. Eliceiri, S. M. Trier, and P. J. Keely, Biophys. J. **95**, 5374 (2008).

[13] T. R. Cox and J. T. Erler, Dis. Model. Mech. **4**, 165 (2011).

[14] J. Kim, X. Mao, C. A. R. Jones, J. Feng, B. Sun, L. M. Sander, and H. Levine, Nat. Commun. **8**, (2017).

[15] H. Wang, A. S. S. Abhilash, C. S. S. Chen, R. G. G. Wells, and V. B. B. Shenoy, Biophys. J. **107**, 2592 (2015).

[16] R. K. Sawhney and J. Howard, J. Cell Biol. **157**, 1083 (2002).

[17] C. A. R. Jones, M. Cibula, J. Feng, E. A. Krnacik, D. H. McIntyre, H. Levine, and B. Sun, Proc. Natl. Acad. Sci. **112**, E5117 (2015).

[18] Y. L. Han, P. Ronceray, G. Xu, A. Malandrino, R. D. Kamm, M. Lenz, C. P. Broedersz, and M. Guo, Proc. Natl. Acad. Sci. U. S. A. **115**, 4075 (2018).

[19] X. Ma, M. E. Schickel, M. D. Stevenson, A. L. Sarang-Sieminski, K. J. Gooch, S. N. Ghadiali, and R. T. Hart, Biophys. J. **104**, 1410 (2013).

[20] Q. Shi, R. P. Ghosh, H. Engelke, C. H. Rycroft, L. Cassereau, J. A. Sethian, V. M. Weaver, and J. T. Liphardt, Proc. Natl. Acad. Sci. **111**, 658 (2014).

[21] L. Liang, C. Jones, S. Chen, B. Sun, and Y. Jiao, Phys. Biol. **13**, (2016).

[22] P. Ronceray, C. Broedersz, and M. Lenz, Proc. Natl. Acad. Sci. **113**, 2827 (2015).

[23] T. Lecuit, P.-F. Lenne, and E. Munro, Annu. Rev. Cell Dev. Biol. **27**, 157 (2011).

[24] R. Fernandez-Gonzalez, S. de M. Simoes, J. C. Röper, S. Eaton, and J. A. Zallen, Dev. Cell **17**, 736 (2009).

[25] G. Totsukawa, Y. Wu, Y. Sasaki, D. J. Hartshorne, Y. Yamakita, S. Yamashiro, and F. Matsumura, J. Cell Biol. **164**, 427 (2004).

[26] K. Jakab, A. Neagu, V. Mironov, R. R. Markwald, and G. Forgacs, Proc. Natl. Acad. Sci. **101**, 2864 (2004).

[27] A. D. Doyle, N. Carvajal, A. Jin, K. Matsumoto, and K. M. Yamada, Nat. Commun. **6**, (2015).

[28] F. Beroz, L. M. Jawerth, S. Münster, D. A. Weitz, C. P. Broedersz, and N. S. Wingreen, Nat. Commun. **8**, (2017).

[29] A. A. Alobaidi, Y. Xu, S. Chen, Y. Jiao, and B. Sun, Phys. Biol. **14**, (2017).

[30] P. Friedl and D. Gilmour, Nat. Rev. Mol. Cell Biol. **10**, 445 (2009).

[31] M. A. Wozniak and C. S. Chen, Nat. Rev. Mol. Cell Biol. **10**, 34 (2009).

[32] D. E. Jaalouk and J. Lammerding, Nat. Rev. Mol. Cell Biol. **10**, 63 (2009).

[33] M. E. Lukashev and Z. Werb, Trends Cell Biol. **8**, 437 (1998).

[34] R. Sunyer, V. Conte, J. Escribano, A. Elosegui-Artola, A. Labernadie, L. Valon, D. Navajas, J. M. García-Aznar, J. J. Muñoz, P. Roca-Cusachs, and X. Trepat, Science (80-. ). **353**, 1157 (2016).

[35] S. R. Gujarathi, C. L. Farrow, C. Glosser, L. Granlund, and P. M. Duxbury, Phys. Rev. E - Stat. Nonlinear, Soft Matter Phys. **89**, (2014).

[36] F. J. O'Brien, B. a Harley, M. a Waller, I. V Yannas, L. J. Gibson, and P. J. Prendergast, Technol. Health Care **15**, 3 (2007).

[37] Y. L. Yang, S. Motte, and L. J. Kaufman, Biomaterials **31**, 5678 (2010).

[38] A. G. Ogston, Trans. Faraday Soc. **54**, 1754 (1958).

[39] A. Takahashi, R. Kita, T. Shinozaki, K. Kubota, and M. Kaibara, Colloid Polym. Sci. **281**, 832 (2003).

[40] W. Mickel, S. Münster, L. M. Jawerth, D. A. Vader, D. A. Weitz, A. P. Sheppard, K. Mecke, B. Fabry, and G. E. Schröder-Turk, Biophys. J. **95**, 6072 (2008).

[41] Y. Jiao and S. Torquato, Phys. Biol. **9**, (2012).

[42] A. O. Brightman, B. P. Rajwa, J. E. Sturgis, M. E. McCallister, J. P. Robinson, and S. L. Voytik-Harbin, Biopolymers **54**, 222 (2000).

[43] J. Zhu and L. J. Kaufman, Biophys. J. **106**, 1822 (2014).

[44] S. B. Lindström, D. A. Vader, A. Kulachenko, and D. A. Weitz, Phys. Rev. E - Stat. Nonlinear, Soft Matter Phys. **82**, (2010).

[45] C. A. R. Jones, L. Liang, D. Lin, Y. Jiao, and B. Sun, Soft Matter **10**, 8855 (2014).

[46] T. Stylianopoulos, B. Diop-Frimpong, L. L. Munn, and R. K. Jain, Biophys. J. **99**, 3119 (2010).

[47] A. G. Ogston, B. N. Preston, and J. D. Wells, Proc. R. Soc. A Math. Phys. Eng. Sci. **333**, 297 (1973).

[48] L. Johansson, C. Elvingson, and J. E. Loefroth, Macromolecules **24**, 6024 (1991).

[49] L. Johansson and J.-E. Löfroth, J. Colloid Interface Sci. **142**, 116 (1991).

[50] L. Johansson, U. Skantze, and J. E. Löfroth, Macromolecules **24**, 6019 (1991).

[51] L. Johansson and J.-E. Löfroth, J. Chem. Phys. **98**, 7471 (1993).

[52] H. A. Leddy, M. A. Haider, and F. Guilak, Biophys. J. **91**, 311 (2006).

[53] A. Erikson, H. N. Andersen, S. N. Naess, P. Sikorski, and C. D. L. Davies, Biopolymers **89**, 135 (2008).

[54] A. P. Chatterjee, J. Phys. Condens. Matter **23**, (2011).

[55] Y. L. Yang, L. M. Leone, and L. J. Kaufman, Biophys. J. **97**, 2051 (2009).

[56] C. B. Raub, A. J. Putnam, B. J. Tromberg, and S. C. George, Acta Biomater. **6**, 4657 (2010).

[57] C. P. Broedersz, X. Mao, T. C. Lubensky, and F. C. Mackintosh, Nat. Phys. **7**, 983 (2011).

[58] J. Feng, H. Levine, X. Mao, and L. M. Sander, Phys. Rev. E. Stat. Nonlin. Soft Matter Phys. **91**, 042710 (2015).

[59] H. Jiang, L. Jiang, J. D. Posner, and B. D. Vogt, Comput. Mech. **42**, 607 (2008).

[60] J. Zhang, X. Zhao, Z. Suo, and H. Jiang, J. Appl. Phys. **105**, (2009).

[61] A. S. Abhilash, B. M. Baker, B. Trappmann, C. S. Chen, and V. B. Shenoy, Biophys. J. **107**, 1829 (2014).

[62] S. Motte and L. J. Kaufman, Biopolymers **99**, 35 (2013).

[63] A. Guzman, M. J. Ziperstein, and L. J. Kaufman, Biomaterials **35**, 6954 (2014).

[64] R. C. Arevalo, P. Kumar, J. S. Urbach, and D. L. Blair, PLoS One **10**, (2015).

[65] C. Heussinger and E. Frey, Eur. Phys. J. E **24**, 47 (2007).

[66] D. A. Head, A. J. Levine, and F. C. MacKintosh, Phys. Rev. E - Stat. Nonlinear, Soft Matter Phys. **72**, (2005).

[67] Y. Shokef and S. A. Safran, Phys. Rev. Lett. **108**, (2012).

[68] J. Notbohm, A. Lesman, P. Rosakis, D. A. Tirrell, and G. Ravichandran, J. R. Soc. Interface **12**, 20150320 (2015).

[69] B. Lee, X. Zhou, K. Riching, K. W. Eliceiri, P. J. Keely, S. A. Guelcher, A. M. Weaver, and Y. Jiang, PLoS One **9**, (2014).

[70] W. Han, S. Chen, W. Yuan, Q. Fan, J. Tian, X. Wang, L. Chen, X. Zhang, W. Wei, R. Liu, J. Qu, Y. Jiao, R. H. Austin, and L. Liu, Proc. Natl. Acad. Sci. **113**, 11208 (2016).

[71] A. Aman and T. Piotrowski, Dev. Biol. (2010).

[72] A. Vaezi, C. Bauer, V. Vasioukhin, and E. Fuchs, Dev. Cell (2002).

[73] S. Werner, T. Krieg, and H. Smola, J. Invest. Dermatol. (2007).

[74] P. Friedl and E. B. Bröcker, Cell. Mol. Life Sci. (2000).

[75] H. Szurmant and G. W. Ordal, Microbiol. Mol. Biol. Rev. (2004).

[76] C. Frantz, K. M. Stewart, and V. M. Weaver, J. Cell Sci. (2010).

[77] H. Mohammadi, P. D. Arora, C. A. Simmons, P. A. Janmey, and C. A. McCulloch, J. R. Soc. Interface (2015).

[78] S. Nam, K. H. Hu, M. J. Butte, and O. Chaudhuri, Proc. Natl. Acad. Sci. (2016).

[79] S. Nam, J. Lee, D. G. Brownfield, and O. Chaudhuri, Biophys. J. (2016).

[80] S. V. Plotnikov, A. M. Pasapera, B. Sabass, and C. M. Waterman, Cell (2012).

[81] S. B. Carter, Nature (1967).

[82] J. H. C. Wang and E. S. Grood, Connect. Tissue Res. (2000).

[83] S. Wang and P. G. Wolynes, Proc. Natl. Acad. Sci. (2012).

[84] L. Ramage, Cell Health Cytoskelet. (2012).

[85] F. Grinnell and W. M. Petroll, Annu. Rev. Cell Dev. Biol. (2010).

[86] T. Angelini, E. Hannezo, X. Trepat, M. Marquez, J. Fredberg, and D. Weitz, Proc. Natl. Acad. Sci. (2011).

[87] P. Friedl, J. Locker, E. Sahai, and J. E. Segall, Nat. Cell Biol. (2012).

[88] M. Poujade, E. Grasland-Mongrain, A. Hertzog, J. Jouanneau, P. Chavrier, B. Ladoux, A. Buguin, and P. Silberzan, Proc. Natl. Acad. Sci. (2007).

[89] M. Rogers, J. Lembong, H. A. Stone, V. Normand, and B. Sun, Proc. Natl. Acad. Sci. (2012).

[90] D. T. Tambe, C. Corey Hardin, T. E. Angelini, K. Rajendran, C. Y. Park, X. Serra-Picamal, E. H. Zhou, M. H. Zaman, J. P. Butler, D. A. Weitz, J. J. Fredberg, and X. Trepat, Nat. Mater. (2011).

[91] E. Theveneau, B. Steventon, E. Scarpa, S. Garcia, X. Trepat, A. Streit, and R. Mayor, Nat. Cell Biol. (2013).

[92] S. Chen, H. Li, and Y. Jiao, Phys. Rev. E - Stat. Nonlinear, Soft Matter Phys. **92**, (2015).

[93] E. Y. Guo, N. Chawla, T. Jing, S. Torquato, and Y. Jiao, Mater. Charact. **89**, 33 (2014).

[94] C. E. Zachary and S. Torquato, Phys. Rev. E - Stat. Nonlinear, Soft Matter Phys. **84**, (2011).

[95] C. L. Y. Yeong and S. Torquato, Phys. Rev. E - Stat. Physics, Plasmas, Fluids, Relat. Interdiscip. Top. **57**, 495 (1998).

[96] C. L. Y. Yeong and S. Torquato, Phys. Rev. E - Stat. Physics, Plasmas, Fluids, Relat. Interdiscip. Top. **58**, 224 (1998).

[97] J. Steinwachs, C. Metzner, K. Skodzek, N. Lang, I. Thievessen, C. Mark, S. Münster, K. E. Aifantis, and B. Fabry, Nat. Methods **13**, 171 (2016).

[98] K. J. Cheung, E. Gabrielson, Z. Werb, and A. J. Ewald, Cell (2013).

[99] N. Aceto, A. Bardia, D. T. Miyamoto, M. C. Donaldson, B. S. Wittner, J. A. Spencer, M. Yu, A. Pely, A. Engstrom, H. Zhu, B. W. Brannigan, R. Kapur, S. L. Stott, T. Shioda, S. Ramaswamy, D. T. Ting, C. P. Lin, M. Toner, D. A. Haber, and S. Maheswaran, Cell (2014).

[100] K. Wolf, Y. I. Wu, Y. Liu, J. Geiger, E. Tam, C. Overall, M. S. Stack, and P. Friedl, Nat. Cell Biol. (2007).

[101] C. Gaggioli, S. Hooper, C. Hidalgo-Carcedo, R. Grosse, J. F. Marshall, K. Harrington, and E. Sahai, Nat. Cell Biol. (2007).

[102] J. Konen, E. Summerbell, B. Dwivedi, K. Galior, Y. Hou, L. Rusnak, A. Chen, J. Saltz, W. Zhou, L. H. Boise, P. Vertino, L. Cooper, K. Salaita, J. Kowalski, and A. I. Marcus, Nat. Commun. (2017).

[103] B. A. Camley, B. Li, Y. Zhao, E. Ben-Jacob, H. Levine, Y. Zhang, and W.-J. Rappel, Proc. Natl. Acad. Sci. (2014).

[104] J. Zimmermann, B. A. Camley, W.-J. Rappel, and H. Levine, Proc. Natl. Acad. Sci. (2016).

[105] Z. S. Dean, P. Elias, N. Jamilpour, U. Utzinger, and P. K. Wong, Anal. Chem. (2016).

[106] N. Yamaguchi, T. Mizutani, K. Kawabata, and H. Haga, Sci. Rep. (2015).

[107] P. P. Provenzano, K. W. Eliceiri, J. M. Campbell, D. R. Inman, J. G. White, and P. J. Keely, BMC Med. (2006).

[108] M. W. Conklin, J. C. Eickhoff, K. M. Riching, C. A. Pehlke, K. W. Eliceiri, P. P. Provenzano, A. Friedl, and P. J. Keely, Am. J. Pathol. (2011).

[109] H. Acloque, M. S. Adams, K. Fishwick, M. Bronner-Fraser, and M. A. Nieto, J. Clin. Invest. (2009).

[110] J. M. Lee, S. Dedhar, R. Kalluri, and E. W. Thompson, J. Cell Biol. (2006).

[111] S. Chen, Y. Zheng, J. Kim, H. Nan, Y. Jiao, B. Sun, and W. Xu, Phys. Biol. (2019).

[112] J. Kim, J. Feng, C. A. R. Jones, X. Mao, L. M. Sander, H. Levine, and B. Sun, Nat. Commun. **8**, (2017).

[113] M. Dietrich, H. Le Roy, D. B. Brückner, H. Engelke, R. Zantl, J. O. Rädler, and C. P. Broedersz, Soft Matter (2018).

[114] B. D. Lubachevsky and F. H. Stillinger, J. Stat. Phys. **60**, 561 (1990).

[115] S. Torquato, T. M. Truskett, and P. G. Debenedetti, Phys. Rev. Lett. (2000).

[116] H. Nan, L. Liang, G. Chen, L. Liu, R. Liu, and Y. Jiao, Phys. Rev. E **97**, 033311 (2018).

[117] W. Xu, X. Su, and Y. Jiao, Phys. Rev. E (2016).

[118] M. D. Rintoul and S. Torquato, J. Phys. A. Math. Gen. **30**, L585 (1997).

[119] T. Vicsek, A. Czirk, E. Ben-Jacob, I. Cohen, and O. Shochet, Phys. Rev. Lett. (1995).

[120] J. M. Belmonte, G. L. Thomas, L. G. Brunnet, R. M. C. De Almeida, and H. Chaté, Phys. Rev. Lett. (2008).

[121] I. Tadeo, A. P. Berbegall, S. Navarro, V. Castel, and R. Noguera, Pediatr. Blood Cancer (2017).

[122] A. Schaefer and P. L. Hordijk, J. Cell Sci. (2015).

[123] L. Dupré, R. Houmadi, C. Tang, and J. Rey-Barroso, Front. Immunol. (2015).

[124] M. Hammerman, P. Blomgran, A. Dansac, P. Eliasson, and P. Aspenberg, J. Appl. Physiol. (2017).